Check for updates

JIPB Journal of Integrative Plant Biology

Research Article
https://doi.org/10.1111/jipb.70081

Check for updates

Phosphorylation fine-tunes ceramide synthase activity and stability to modulate sphingolipid biosynthesis and immune responses

Kun Zhang[1], Yi-Li Chen[1], Jia-Ting Lin[1], Zi-Xin Lu[1], Yu-Bing Yang[1], Yong-Kang Li[1], Chang Yang[1], Jia Lin[1], Shuai-Kang Liu[1], Ling-Yan Wang[1], Hong-Yun Zeng[2]* and Nan Yao[1]*

1. Guangdong Provincial Key Laboratory of Plant Stress Biology, State Key Laboratory of Biocontrol, School of Life Sciences, Sun Yat-sen University, Guangzhou 510275, China
2. Institute of Fruit Tree Research, Guangdong Academy of Agricultural Sciences; Key Laboratory of South Subtropical Fruit Biology and Genetic Resource Utilization, Ministry of Agriculture and Rural Affairs; Guangdong Provincial Key Laboratory of Science and Technology Research on Fruit Tree, Guangzhou 510640, China
*Correspondences: Hong-Yun Zeng (zenghongyun@gdaas.cn); Nan Yao (yaonan@mail.sysu.edu.cn, Dr. Yao is fully responsible for the distribution of all materials associated with this article)

Kun Zhang

Nan Yao

ABSTRACT

Ceramide synthases (CerSs) are central to sphingolipid biosynthesis and influence plant development and defense responses. However, how CerS activity is regulated in plants remains unclear. Here, we discovered that LAG ONE HOMOLOG 2 (LOH2), the sole long-chain CerS in Arabidopsis (*Arabidopsis thaliana*), is post-translationally regulated by the ubiquitous kinase casein kinase 2 (CK2). CK2 interacts with LOH2 and phosphorylates serine residues S289 and S291 within its C-terminal region. We mutated these two serines to alanines and expressed the resulting non-phosphorylatable LOH2 variant in transgenic plants and protoplasts. We found that phosphorylation enhances LOH2 enzymatic activity, partially by increasing its substrate-binding affinity, but concurrently promotes LOH2 polyubiquitination and degradation via the 26S proteasome without affecting its subcellular localization. Plants expressing a non-phosphorylatable LOH2 variant showed diminished cell death, reduced C16 ceramide biosynthesis and salicylic acid (SA) accumulation, and compromised resistance to the fungal toxin Fumonisin B1 and the bacterial pathogen *Pseudomonas syringae*. Pathogen infection induces LOH2 phosphorylation, promoting C16 ceramide accumulation, SA production, and resistance gene expression. Collectively, our findings demonstrate that CK2 fine-tunes LOH2 enzymatic activity and stability, and thus the production of long-chain ceramides through phosphorylation, thereby regulating plant development and defense responses.

Keywords: Arabidopsis, casein kinase 2, ceramide, enzymatic activity, LOH2, phosphorylation, plant immunity, stability

Zhang K, Chen Y.-L., Lin J.-T., Lu, Z.-X., Yang, Y.-B., Li, Y.-K., Yang, C., Lin, J., Liu, S.-K., Wang, L.-Y., et al. (2025) Phosphorylation fine-tunes ceramide synthase activity and stability to modulate sphingolipid biosynthesis and immune responses. J. Integr. Plant Biol. **00:** 1–19.

INTRODUCTION

Ceramides (Cers) are composed of fatty acids linked by amide bonds to a sphingoid base backbone and are categorized as long chain (C16 or C18) or very long chain (≥ C20), depending on the length of the fatty acid chain (Markham et al., 2011; Ternes et al., 2011; Luttgeharm et al., 2015). Ceramides are present in all eukaryotic organisms, where they serve as the building blocks of all complex sphingolipids. In plants, Cers are critical signaling molecules that regulate growth, programmed cell death, and responses to biotic and abiotic stress

© 2025 Institute of Botany, Chinese Academy of Sciences.

(Luttgeharm et al., 2015; Ali et al., 2018; Liu et al., 2021; Cahoon et al., 2024).

Ceramides are primarily biosynthesized by ceramide synthase (CerS) enzymes. The budding yeast *Saccharomyces cerevisiae* contains two functionally redundant CerS enzymes, Longevity-assurance gene Cognate 1 (Lac1p) and Longevity-assurance gene 1 (Lag1p), as well as their regulatory subunit Lag1p/Lac1p Interacting Protein 1 (Lip1p), with C26-Coenzyme A (CoA) being the preferred acyl-CoA substrate (Megyeri et al., 2019; Xie et al., 2023). The six mammalian CerS enzymes (CerS1–CerS6) show characteristic substrate selectivity toward acyl-CoAs with different chain lengths (Laviad et al., 2008; Sassa et al., 2016). Arabidopsis (*Arabidopsis thaliana*) has two classes of CerS enzymes: Class I and Class II. The Class I enzyme LAG ONE HOMOLOG 2 (LOH2) produces long-chain Cers, whereas the Class II enzymes LOH1 and LOH3 produce very-long-chain Cers (Markham et al., 2011; Ternes et al., 2011; Luttgeharm et al., 2015, 2016; Zeng and Yao, 2022).

Very-long-chain Cers typically play crucial roles in plant growth and development (Markham et al., 2011; Zeng et al., 2020), whereas long-chain Cers are strongly linked to cell death and immune responses (Bi et al., 2014; Luttgeharm et al., 2015). LOH1 and LOH3 are functionally redundant; in Arabidopsis, their simultaneous absence leads to an almost complete lack of very-long-chain fatty acid sphingolipids and severely impaired growth and development (Markham et al., 2011). Overexpression of *LOH1* or *LOH3* promoted cell differentiation and root growth and increased plant biomass, despite resulting in only a slight increase in very-long-chain fatty acid Cer levels (Luttgeharm et al., 2015). By contrast, loss of LOH2 function caused no clear developmental defects in Arabidopsis (Markham et al., 2011), whereas *LOH2* overexpression caused extreme overaccumulation of C16 Cers and salicylic acid (SA), leading to dwarfing and cell death (Luttgeharm et al., 2015).

The fungal toxin Fumonisin B1 (FB1) is derived from *Fusarium moniliforme* Sheld and inhibits CerS owing to its structural similarity to long-chain bases (LCBs). FB1 is widely used to study the effects of CerS inhibition on sphingolipid metabolism and signaling in eukaryotes (Zeng et al., 2020; Pascoa et al., 2024; Zhang et al., 2024). Fumonisin B1 treatment induces the accumulation of LCBs and C16 Cers in Arabidopsis (Markham et al., 2011; Zeng et al., 2022). Plants overexpressing *LOH2* or *LOH3* showed increased resistance to FB1, whereas *LOH1*-overexpressing plants did not, suggesting that LOH1 was most strongly inhibited by FB1 (Markham et al., 2011; Luttgeharm et al., 2015, 2016). However, despite the significant roles of LOHs, the regulatory mechanisms underlying their functions remain to be fully characterized.

Post-translational modifications, such as phosphorylation and dephosphorylation mediated by protein kinases and phosphatases, modulate protein function and stability in eukaryotes (Vu et al., 2018). Casein kinase 2 (CK2), a highly conserved serine/threonine protein kinase found in eukaryotes, has unique structural and biochemical characteristics (Niefind et al., 2001; Mulekar and Huq, 2014). In yeast and mammals, CK2 forms a heterotetrameric complex comprising two catalytic subunits (α and/or α′) and two regulatory subunits (β) (Padmanabha et al., 1990; Niefind et al., 2001). In plants, CK2 is typically encoded by multiple genes and exists in both monomeric and oligomeric forms *in vivo* (Klimczak et al., 1995; Mulekar and Huq, 2014; Wang et al., 2022). Four genes encoding α subunits of CK2 and four genes encoding β subunits have been identified in Arabidopsis (Salinas et al., 2006).

In plants, CK2 is an essential housekeeping kinase that functions in regulating various processes such as light signaling and circadian rhythms, and in maintaining normal growth and development (Mulekar and Huq, 2014). Casein kinase 2 also plays significant roles in plant responses to various biotic and abiotic stresses. For example, in rice (*Oryza sativa*), CK2 phosphorylates the TGA family transcription factor OsTGA5, thereby alleviating its repression of downstream resistance genes and enhancing rice blast resistance (Niu et al., 2022). Zhu et al. (2023a) reported that CK2 promotes the response to jasmonic acid signaling by phosphorylating MYC2 in Arabidopsis. By contrast, CKα4 suppresses SA accumulation to negatively regulate plant resistance to hemibiotrophic pathogens (Rui et al., 2024). Casein kinase 2 participates in abscisic acid responses and stem cell exhaustion under aluminum toxicity and phosphate deficiency (Wei et al., 2021; Zhang et al., 2022a). Although CK2 regulates various essential physiological processes, its potential role in plant sphingolipid metabolism has not been investigated previously.

Here, we show that CK2 phosphorylates Arabidopsis LOH2 at the serine residues S289 and S291 and that pathogen infection promotes CK2 phosphorylation activity. Phosphorylation of LOH2 enhanced its activity but reduced its protein stability, thereby affecting growth and programmed cell death, as well as resistance to the fungal toxin FB1 and the bacterial pathogen *Pseudomonas syringae* pv. *maculicola*. Our study reveals a CerS regulatory mechanism that is evolutionarily conserved, yet biochemically distinct from the mechanisms regulating CerS in mammals and yeast, and provides insight into the regulation of sphingolipid biosynthesis during plant development and pathogen defense responses.

RESULTS

Casein kinase 2 promotes the accumulation of C16 Cers

Arabidopsis LOH1, LOH2, and LOH3 are phosphoproteins with phosphorylation sites on three serine (Ser) residues (Ser-300, Ser-302, and Ser-304), two serine residues (Ser-289 and Ser-291), and two serine residues (Ser-298 and Ser-300), respectively, all located in their C-terminal regions (Figure S1A) (Nakagami et al., 2010; Roitinger et al., 2015). As indicated by an amino acid sequence alignment of multiple CerSs

17447909, 0, Downloaded from https://onlinelibrary.wiley.com/doi/10.1111/jipb.70081 by University Of British Columbia, Wiley Online Library on [27/01/2026]. See the Terms and Conditions (https://onlinelibrary.wiley.com/terms-and-conditions) on Wiley Online Library for rules of use; OA articles are governed by the applicable Creative Commons License

(Figure S1B), the first serine residue (Ser-300 of LOH1, Ser-289 of LOH2, and Ser-298 of LOH3) is the most conserved across yeast, mice, humans, and plants. All serine phosphorylation sites in Arabidopsis LOH match the consensus sequence for CK2 phosphorylation, that is (S/T)XX(D/E) (Sassa et al., 2016; Zhu et al., 2023a). The serine residues that are phosphorylated in Arabidopsis LOH are also present in CerS-related proteins from other plant species, including rapeseed (*Brassica napus*), tomato (*Solanum lycopersicum*), tree cotton (*Gossypium arboreum*), rice (*Oryza sativa*), yuzu (*Citrus junos*), apple (*Malus domestica*), tea plant (*Camellia sinensis*), rose (*Rosa* sp.), maize (*Zea mays*), and foxtail millet (*Setaria italica*) (Figure S1B). These plant CerS homologs fall into two clusters in the phylogenetic tree: the first contains proteins that are more closely related to LOH2, whereas the second contains proteins that are more closely related to LOH1 and LOH3 (Figure S2). With the exception of the Class I CerS homolog in maize, which lacks the C-terminal region, and OsASC1L2 in *Oryza sativa*, all other plant CerSs possess the (S/T)XX(D/E) motif (Figures S1B, S2), indicating that this motif is highly conserved in plants.

Because all Arabidopsis LOHs possess putative CK2 motifs, we investigated whether CK2 influences Cer biosynthesis by phosphorylating LOHs. Lu et al. (2011b) reported that loss of function of three out of the four CK2α subunits in Arabidopsis caused an ~70% decrease in bulk CK2 kinase activity compared with that of the wild type (WT). We analyzed the sphingolipid profiles of 4-week-old WT and *ckα1 ckα2 ckα3* triple-mutant plants and observed no significant differences in total LCB, Cer, hydroxyceramide (hCer), or glucosylceramide (GlcCer) contents compared with those of WT plants (Figure S3; Dataset S1). However, the *ckα1 ckα2 ckα3* triple mutant accumulated significantly lower levels of C16 Cers (mainly t18:0 c16:0 and t18:1 c16:0) (Figure 1A) and h16 GlcCers (all individual h16 GlcCer species) (Figure 1B) than the WT. These results suggest that CK2 modulates the biosynthesis of Cers, particularly C16 Cers.

Casein kinase 2 interacts with and phosphorylates LOH2

LOH2 is primarily responsible for the biosynthesis of C16 Cers (Ternes et al., 2011; Luttgeharm et al., 2015). To investigate whether LOH2 is a substrate of CK2, we used bimolecular fluorescence complementation (BiFC) assays to examine the potential interactions of LOH2 with individual CK2 subunits. We detected no evidence of interactions between LOH2 and the CK2 subunits CKα2, CKα3, CKα4, CKβ2, CKβ3, or CKβ4 (Figure S4). However, LOH2 interacted with CKα1 and CKβ1 (Figure 2A). To investigate LOH2 interaction partners *in planta*, we generated stable transgenic

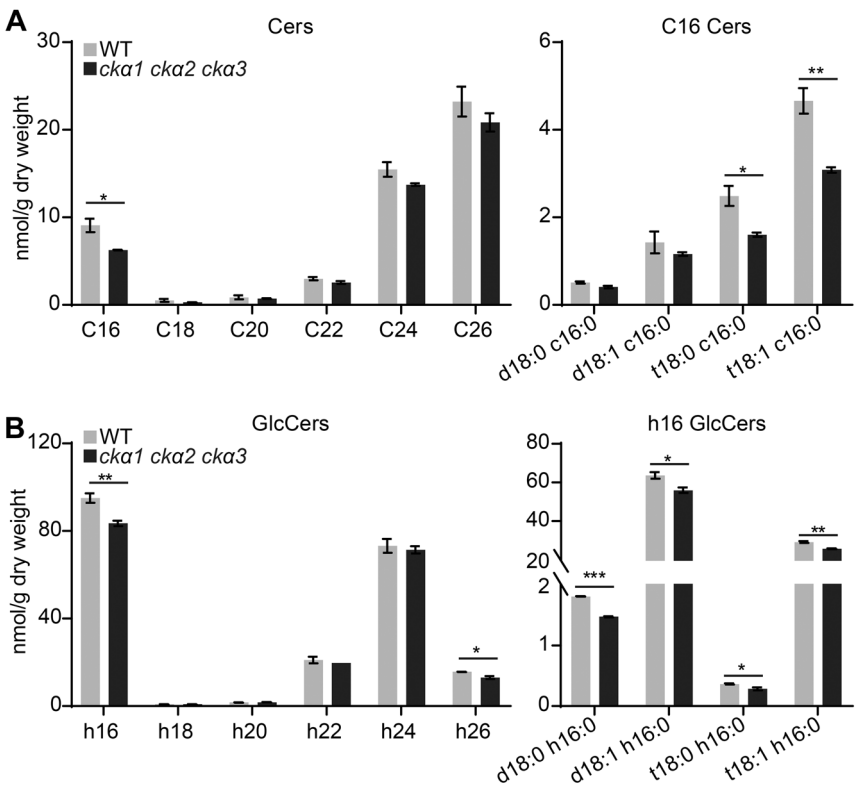

Figure 1. Casein kinase 2 promotes the accumulation of C16 Cers

(A) Contents of ceramide (Cer) species with various fatty acid moieties and various C16 Cer species. **(B)** Contents of glucosylceramide (GlcCer) species with various fatty acid moieties and various h16 GlcCer species. Values are means ± standard error (*SE*) ($n = 3$ independent samples). Sphingolipids were extracted from the rosettes of 4-week-old soil-grown wild-type (WT) and *ckα1 ckα2 ckα3* plants. Significant differences were determined using a two-tailed Student's *t*-test (*$P < 0.05$; **$P < 0.01$; ***$P < 0.001$).

17447909, 0, Downloaded from https://onlinelibrary.wiley.com/doi/10.1111/jipb.70081 by University Of British Columbia, Wiley Online Library on [27/01/2026]. See the Terms and Conditions (https://onlinelibrary.wiley.com/terms-and-conditions) on Wiley Online Library for rules of use; OA articles are governed by the applicable Creative Commons License

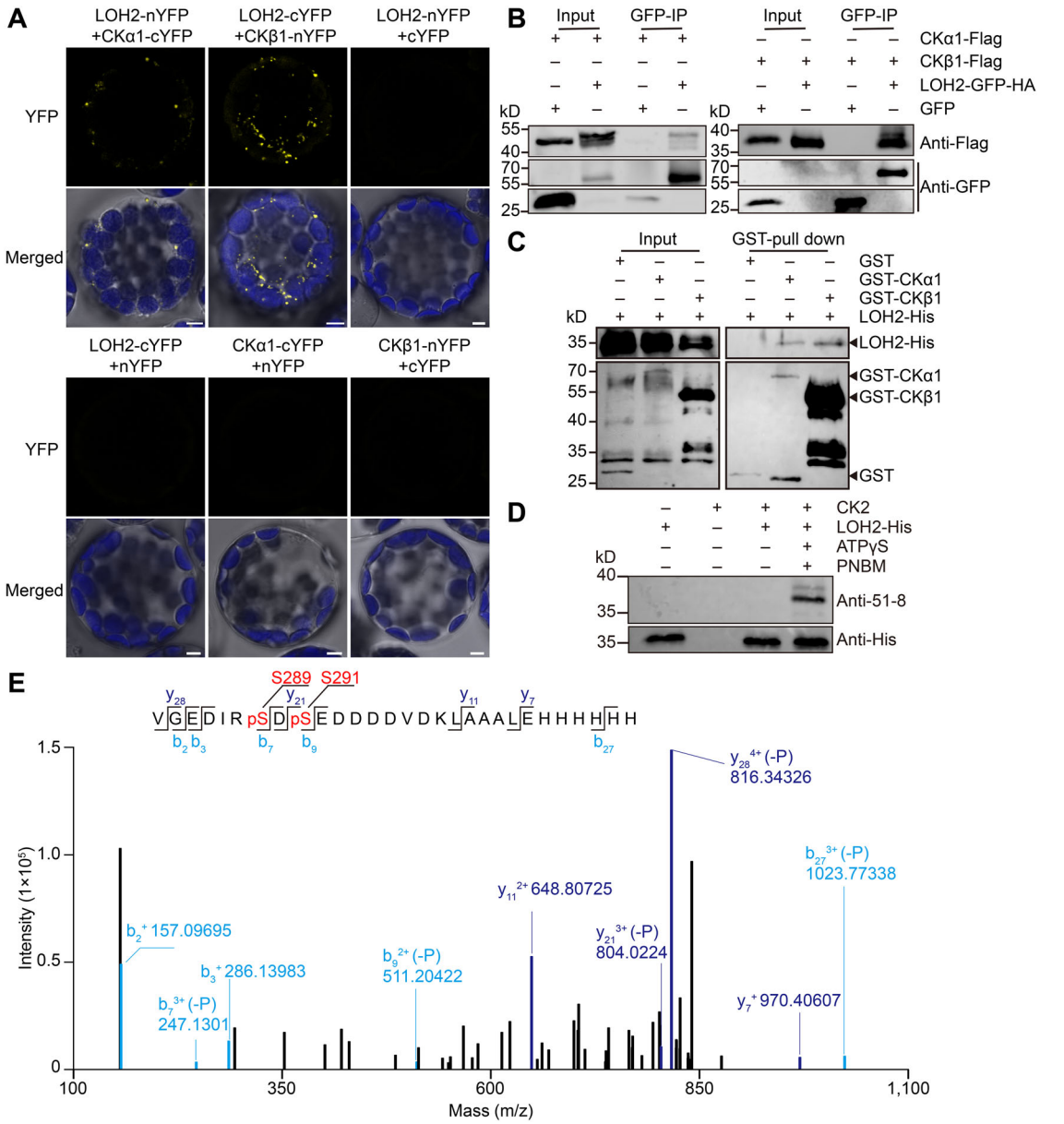

Figure 2. CK2 interacts with and phosphorylates LOH2

(A) Bimolecular fluorescence complementation (BiFC) assay testing the interactions between CK2 subunits (CKα1 or CKβ1) and LOH2. The constructs *LOH2-nYFP* and *CKα1-cYFP*, *LOH2-cYFP* and *CKβ1-nYFP*, *LOH2-nYFP,* and *cYFP*, *LOH2-cYFP* and *nYFP*, *CKα1-cYFP* and *nYFP*, or *CKβ1-nYFP* and *cYFP* were co-transfected into wild-type (WT) protoplasts, and photos were taken by confocal microscopy at 16 h after transfection. Empty vectors were used as negative controls. Merged images show YFP (yellow), chlorophyll autofluorescence (blue), and bright-field signals. Scale bars, 4 μm. The interactions between other subunits of CK2 (CKα2, CKα3, CKα4, CKβ2, CKβ3, and CKβ4) and LOH2 are shown in Figure S4. **(B)** Co-immunoprecipitation (Co-IP) assay of the interaction between CK2 (CKα1 or CKβ1) and LOH2. The constructs *CKα1-Flag* or *CKβ2-Flag* were transfected into protoplasts isolated from *35S:GFP* or *LOH2pro:LOH2:GFP:HA* plants, and protein complexes were immunoprecipitated with anti-GFP beads. Free GFP and LOH2-GFP-HA were detected with an anti-GFP antibody; precipitated CKα1-Flag and CKβ2-Flag were detected with an anti-flag antibody. "+" or "−" denotes the presence or absence of the protein in each sample. Free GFP was used as a negative control. **(C)** *In vitro* pull-down assay showing the interactions of LOH2 with CKα1 and CKβ1. Recombinant purified glutathione S-transferase (GST), GST-CKα1, or GST-CKβ1 was incubated with LOH2-His. Following pull-down with GST beads, the proteins were separated by sodium dodecyl sulfate polyacrylamide agarose gel electrophoresis (SDS-PAGE) and subjected to immunoblot analysis with an anti-His antibody. **(D)** Phosphorylation of LOH2 by CK2 *in vitro*. Recombinant purified LOH2-His was incubated with purchased human glioblastoma recombinant CK2 (NEB) in a CK2 reaction buffer containing ATPγS and *p*-nitrobenzyl mesylate (PNBM) and separated by SDS-PAGE. Phosphorylated LOH2-His was detected with anti-thiophosphate ester rabbit monoclonal antibodies (anti-51-8); recombinant purified LOH2-His was detected with an anti-His antibody. Reactions lacking the specified components (–) were used as controls. **(E)** Mass spectrometry identifies Ser-289 and Ser-291 as CK2-mediated phosphorylation sites in LOH2. Recombinant purified LOH2-His was incubated with human glioblastoma recombinant CK2 (NEB) and subjected to mass spectrometry. The amino acid residues highlighted in red are the phosphorylation sites detected in this study. Experiments in **(A–D)** were repeated at least two times with independent samples.

17447909, 0, Downloaded from https://onlinelibrary.wiley.com/doi/10.1111/jipb.70081 by University Of British Columbia, Wiley Online Library on [27/01/2026]. See the Terms and Conditions (https://onlinelibrary.wiley.com/terms-and-conditions) on Wiley Online Library for rules of use; OA articles are governed by the applicable Creative Commons License

Arabidopsis lines harboring the *LOH2pro:LOH2:GFP:HA* transgene in the WT background (Figure S5) and carried out co-immunoprecipitation (Co-IP) assays. When we transfected protoplasts prepared from this *LOH2pro:LOH2:GFP:HA* line with constructs encoding Flag-tagged CKα1 or CKβ1 (*CKα1-Flag* and *CKβ1-Flag*), we detected CKα1-Flag and CKβ1-Flag among the co-precipitated proteins after immunoprecipitation of GFP-tagged LOH2 (LOH2-GFP-HA) (Figure 2B). We performed *in vitro* pull-down assays using the recombinant purified glutathione S-transferase (GST) fusions GST-CKα1 and GST-CKβ1 with LOH2-His, and found that GST-CKα1 and GST-CKβ1, but not GST alone, pulled down LOH2-His (Figure 2C). These results suggest that CKα1 and CKβ1 interact with LOH2 *in vitro* and *in vivo*.

Because LOH1 and LOH3 also contain potential CK2 phosphorylation sites, we examined their interactions with CK2 using BiFC and yeast two-hybrid assays. We found that none of the eight CK2 subunits interacted with LOH1 or LOH3 (Figure S6). These results are consistent with the lack of significant change in very-long-chain Cer levels in the *ckα1 ckα2 ckα3* triple mutant (Figure 1A).

To test whether LOH2 might be a substrate for CK2-mediated phosphorylation, we purified recombinant LOH2-His and performed *in vitro* phosphorylation assays using commercially available human glioblastoma recombinant CK2. Indeed, CK2 phosphorylated LOH2 in the presence of ATPγS and *p*-nitrobenzyl mesylate *in vitro* (Figure 2D). To identify which residues are phosphorylated by CK2, we subjected phosphorylated LOH2-His to mass spectrometry analysis. We detected two phosphorylated residues in LOH2, S289, and S291 (Figure 2E), indicating that these two sites are phosphorylated by CK2.

LOH2 phosphorylation promotes spontaneous cell death and biosynthesis of C16 fatty acid-containing sphingolipids

To confirm the phosphorylation sites of LOH2 *in vivo*, we overexpressed the *35S:LOH2:GFP:HA* (designated *LOH2* OE) construct in the WT background (Figure S7A) and performed phosphoproteomic analysis, again identifying phosphorylation at serine residues S289 and S291 (Figure S7B; Dataset S2). To investigate the functional significance of S289 and S291 phosphorylation, we simultaneously mutated these two amino acids to alanine (S289A, S291A) to generate a non-phosphorylatable form of LOH2. We then overexpressed the *35S:LOH2^{S289A,S291A}:GFP:HA* construct (designated *LOH2^{S289A,S291A}*-OE) in the WT background (Figure S7C). We chose two lines harboring each construct (*LOH2*-OE #12 and *LOH2^{S289A,S291A}*-OE #18 as one group and *LOH2*-OE #10 and *LOH2^{S289A,S291A}*-OE #7 as the other group) for further analysis (Figure S7A, C).

Compared with the WT, *LOH2*-OE #12 seedlings had significantly shorter roots (Figure 3A) and showed a spontaneous cell death phenotype (Figure 3B, C). Compared with *LOH2*-OE #12, *LOH2^{S289A,S291A}*-OE #18 plants displayed phenotypes intermediate between those of the WT and *LOH2*-OE, with greater root growth (Figure 3A) and less severe cell death (Figure 3B, C). Notably, the high expression level of *PATHOGENESIS-RELATED PROTEIN 1* (*PR1*) observed in *LOH2*-OE #12 was completely abolished in *LOH2^{S289A,S291A}*-OE #18 plants, returning to the low levels of the WT, although both lines had similarly increased *LOH2* transcript levels (Figure 3D). The *LOH2*-OE #12 plants also accumulated high levels of free SA and SA glucoside (SAG). By contrast, levels of these compounds were much lower in *LOH2^{S289A,S291A}*-OE #18 plants: SA levels were approximately 50% of those in *LOH2*-OE and SAG levels were as low as those of the WT (Figure 3E). Thus, preventing S289 and S291 phosphorylation in LOH2 in transgenic plants appeared to compromise the ability of this enzyme to regulate plant immunity.

To specifically examine the effects of LOH2 phosphorylation at S289 and S291 on sphingolipid biosynthesis, we measured the sphingolipid contents of WT, *LOH2*-OE #12, and *LOH2^{S289A,S291A}*-OE #18 plants (Dataset S3). Compared with the WT, *LOH2*-OE #12 contained approximately three times more total Cers, especially C16 Cers (Figure 3F). Levels of total hCers, h16 hCers, h16 GlcCers, total GIPCs, and h16 GIPCs were also significantly higher in *LOH2*-OE #12 plants than in the WT (Figures 3G, S8A). Compared with those in *LOH2*-OE #12, levels of these sphingolipids were much lower in *LOH2^{S289A,S291A}*-OE #18 and closer to those in the WT (Figure 3F, G), suggesting that LOH2 function is enhanced by phosphorylation. Surprisingly, compared with WT and *LOH2*-OE #12 plants, *LOH2^{S289A,S291A}*-OE #18 plants accumulated abnormally high levels of LCBs, particularly t18:0 and t18:1 species (Figure S8B). Perhaps, these CerS substrates reached higher levels due to a compromised ability of LOH2^{S289A,S291A} to convert LCBs into Cers. We obtained similar results for the other two lines: *LOH2*-OE #10 and *LOH2^{S289A,S291A}*-OE #7 (Figure S9).

To further explore the functions of LOH2 and LOH2^{S289A,S291A}, we crossed *LOH2*-OE #12 and *LOH2^{S289A,S291A}*-OE #18 with *loh2-2* mutants and obtained homozygous plants, *LOH2*-OE-*loh2-2* and *LOH2^{S289A,S291A}*-OE-*loh2-2* (Figure S10A–C). Compared with WT and *loh2-2* plants, *LOH2*-OE-*loh2-2* plants showed dwarfism and cell death. By contrast, *LOH2^{S289A,S291A}*-OE-*loh2-2* plants showed no discernible phenotypic differences from WT and *loh2-2* plants (Figure S10A). Sphingolipid profiling revealed that *LOH2* expression rescued the deficiency in C16 fatty acid-containing sphingolipids in the *loh2-2* mutants, whereas *LOH2^{S289A,S291A}* did not (Figure S10D, E; Dataset S4). Plants overexpressing *LOH2* in the *loh2-2* background showed increased SA contents, but the SA contents of plants expressing *LOH2^{S289A,S291A}* did not differ significantly from that of the WT and *loh2-2* mutants (Figure S10F). These data demonstrate that phosphorylation at S289 and S291 plays an important role in LOH2 function, affecting the biosynthesis of C16 fatty acid-containing sphingolipids.

17447909, 0, Downloaded from https://onlinelibrary.wiley.com/doi/10.1111/jipb.70081 by University Of British Columbia, Wiley Online Library on [27/01/2026]. See the Terms and Conditions (https://onlinelibrary.wiley.com/terms-and-conditions) on Wiley Online Library for rules of use; OA articles are governed by the applicable Creative Commons License

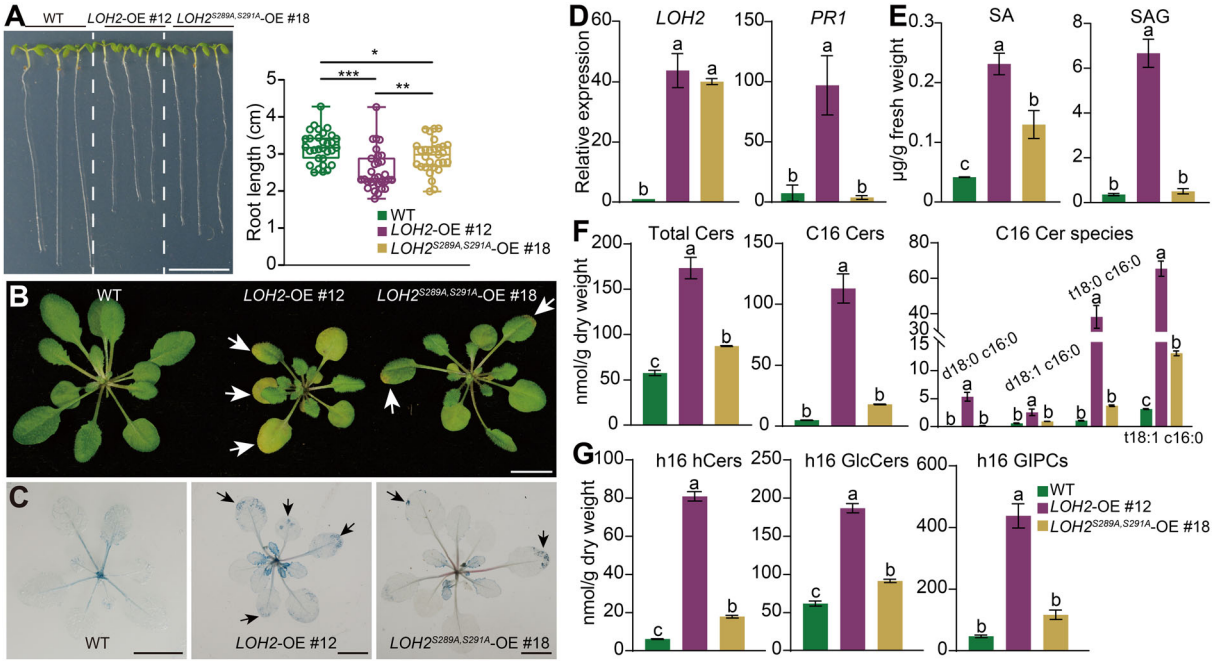

Figure 3. Phosphorylation of LOH2 affects plant growth and cell death

(A) Representative images of 9-d-old seedlings grown on half-strength Murashige and Skoog (1/2MS) medium (left) and root length (right). Values are means ± standard error (*SE*) ($n \geq 29$ seedlings per genotype). Significant differences were determined using a two-tailed Student's *t*-test (*$P < 0.05$; **$P < 0.01$; ***$P < 0.001$). **(B)** Representative photograph of 4-week-old wild type (WT), *LOH2*-overexpressing (*LOH2*-OE #12), and $LOH2^{S289A,S291A}$-overexpressing ($LOH2^{S289A,S291A}$-OE #18) plants. Arrows indicate leaves showing cell death. **(C)** Images of trypan blue staining of the 4-week-old plants shown in **(B)**. Arrows indicate leaf regions showing cell death. **(D)** Relative expression levels of *LOH2* and *PR1* in 4-week-old WT, *LOH2*-OE, and $LOH2^{S289A,S291A}$-OE plants. *ACT2* transcript levels were used as an internal reference. Expression levels were normalized to WT levels, which were set to 1. **(E)** Quantification of free salicylic acid (SA) and SA glucoside (SAG) levels in 4-week-old plants of the indicated genotypes. **(F)** Contents of total ceramides (Cers) (left), total C16 Cers (middle), and various C16 Cer species (right) in 4-week-old plants of the indicated genotypes. **(G)** Contents of total h16 hCers, h16 GlcCers, and h16 GIPCs in 4-week-old plants of the indicated genotypes. Scale bars in **(A–C)**, 1 cm. Values in **(D–G)** are means ± *SE* ($n = 3$ independent samples). Data sets marked with different letters in **(D–G)** indicate significant differences among genotypes assessed using one-way ANOVA, followed by Fisher's LSD test ($P < 0.05$).

Phosphorylation of S289 and S291 enhances LOH2 enzymatic activity

To directly address whether LOH2 function is affected by phosphorylation, we performed *in vitro* CerS activity assays using equal amounts of microsomal proteins isolated from the leaves of WT, *LOH2*-OE #12, and $LOH2^{S289A,S291A}$-OE #18 plants. Microsomal proteins from *LOH2*-OE #12 produced 10.3-fold more d18:0 C16:0 and 25.7-fold more t18:0 C16:0 than WT proteins, whereas $LOH2^{S289A,S291A}$-OE #18 proteins produced a similar amount of d18:0 C16:0 but 4.8-fold more t18:0 C16:0 compared with WT proteins (Figure 4A). We obtained similar results using *LOH2*-OE #10 and $LOH2^{S289A,S291A}$-OE #7: microsomal proteins from *LOH2*-OE #10 produced significantly more d18:0 C16:0 and t18:0 C16:0 than WT and $LOH2^{S289A,S291A}$-OE #7 proteins, whereas microsomal proteins from $LOH2^{S289A,S291A}$-OE #7 produced significantly more t18:0 C16:0 than WT proteins (Figure S11). These results, which are consistent with the sphingolipid profiles of these genotypes, indicate that the catalytic activity of $LOH2^{S289A,S291A}$ is lower than that of intact LOH2.

We next examined the effect of LOH2 phosphorylation status on LOH2 enzymatic activity at protein levels that are closer to endogenous levels. We extracted microsomal proteins from the leaves of *LOH2pro:LOH2:GFP:HA* plants and treated them with λ protein phosphatase (λPPase) to remove phosphorylation marks; we then measured LOH2 activity using d18:0 and C16-CoA as substrates. Treatment with λPPase reduced total LOH2 activity toward d18:0 and C16-CoA by 11.1%, confirming that phosphorylation promotes LOH2 enzymatic activity *in vitro* (Figure 4B). We then transfected protoplasts prepared from *LOH2pro:-LOH2:GFP:HA* plants with *CKα1-Flag* and *CKβ1-Flag* constructs and performed sphingolipid quantification. The presence of CK2 promoted the accumulation of C16 Cers (including d18:0 c16:0 and t18:0 c16:0), h16 hCers, and h16 GlcCers (Figure 4C–E; Dataset S5), demonstrating that CK2 enhances LOH2 enzymatic activity *in vivo*.

To more accurately assess the effect of phosphorylation status on LOH2 enzymatic activity, we performed an *in vivo* CerS assay by measuring sphingolipids in protoplasts prepared from the *loh2-2* mutant (Zeng et al., 2022) transiently transfected with constructs encoding LOH2 or its phosphorylation-site variants (Dataset S6). Protoplasts transfected with *LOH2-Flag* produced 14-fold more C16 Cers than protoplasts transfected with an empty vector control (Figure 4F). $LOH2^{S289A,S291A}$-Flag activity was significantly

17447909, 0, Downloaded from https://onlinelibrary.wiley.com/doi/10.1111/jipb.70081 by University Of British Columbia, Wiley Online Library on [27/01/2026]. See the Terms and Conditions (https://onlinelibrary.wiley.com/terms-and-conditions) on Wiley Online Library for rules of use; OA articles are governed by the applicable Creative Commons License

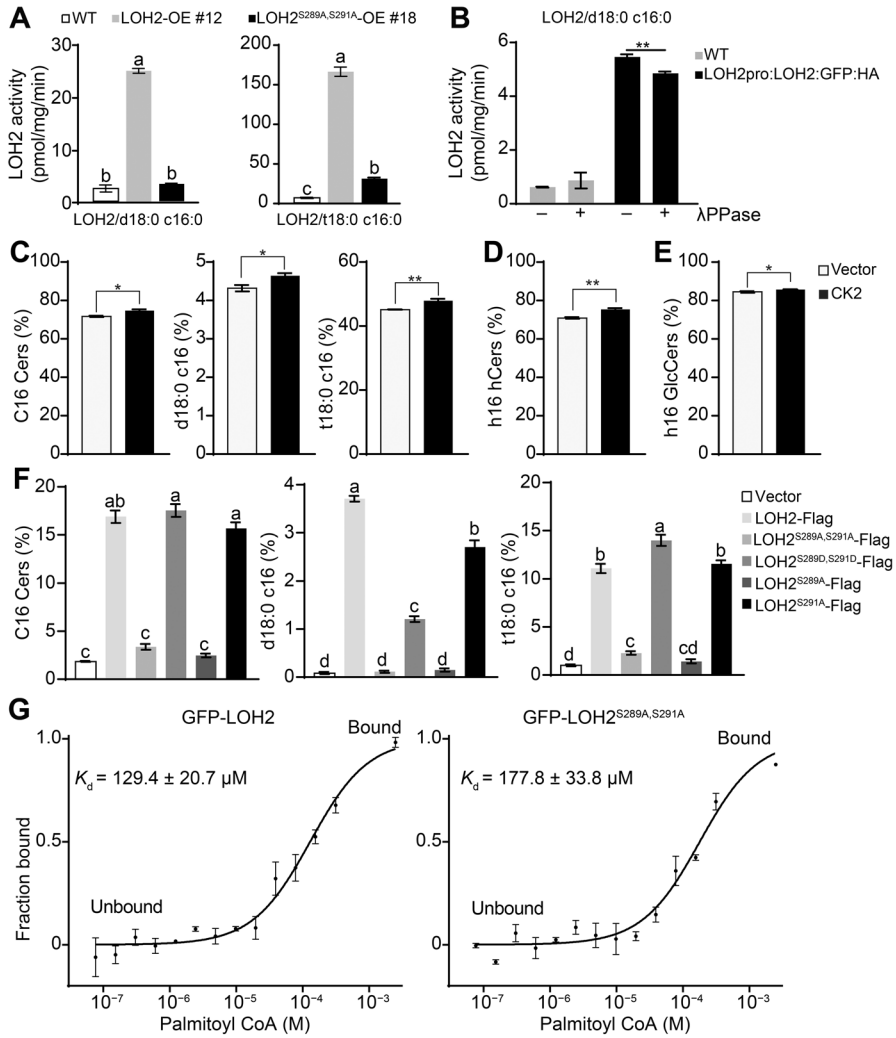

Figure 4. Mutations in the phosphorylation sites of LOH2 decrease its enzymatic activity

(A) *In vitro* activity of LOH2 from the leaves of 4-week-old wild-type (WT), *LOH2*-OE, and *LOH2*^{S289A,S291A}-OE plants. Assays were conducted using 20 μM d18:0 or t18:0 long-chain bases, 50 μM 16:0-CoA, and 10 μg of microsomal protein purified from each genotype at 37°C for 30 min. Sphingolipids were extracted, and d18:0 c16:0 or t18:0 c16:0 were detected by liquid chromatography-mass spectrometry (LC-MS) as described in the Materials and Methods. Values are means ± standard error (*SE*) ($n = 3$ independent assays). **(B)** Effect of λ-protein phosphatase (λPPase) treatment on LOH2 activity. Microsomal proteins (10 μg) prepared from the leaves of WT and *LOH2pro:LOH2:GFP:HA* plants were treated with λPPase as indicated at 30°C for 1 h, followed by incubation with 20 μM d18:0 long-chain bases and 50 μM 16:0-CoA at 37°C for 30 min. Values are means ± *SE* ($n = 3$ independent assays). **(C–E)** CK2 promotes LOH2 enzyme activity *in vivo*. Protoplasts prepared from *LOH2pro:LOH2:GFP:HA plants* were transfected with the plasmids empty vector or CK2 (*CKα1-Flag* and *CKβ1-Flag*). Twenty hours after transfection, sphingolipids were extracted. Values represent the percentage of the contents of C16 ceramides (Cers), d18:0 c16:0, t18:0 c16:0 **(C)**, h16 hCers **(D)**, and h16 GlcCers **(E)** relative to total Cers and are shown as means ± *SE* ($n = 3$). **(F)** *In vivo* activity of LOH2. Protoplasts prepared from *loh2-2* plants were transfected with the plasmids *LOH2-Flag*, *LOH2*^{S289A,S291A}*-Flag*, *LOH2*^{S289D,S291D}*-Flag*, *LOH2*^{S289A}*-Flag*, or *LOH2*^{S291A}*-Flag*. Twenty hours after transfection, sphingolipids were extracted, and the contents of Cers were determined. Values represent the percentage of the contents of C16 Cers, d18:0 c16:0, and t18:0 c16:0 relative to total Cers and are shown as means ± *SE* ($n = 3$). Experiments were repeated three times with independent samples. **(G)** Microscale thermophoresis (MST) assays showing the binding affinity of palmitoyl CoA to GFP-LOH2 and GFP-LOH2^{S289A,S291A}. Graph shows means ± *SE* ($n = 3$ independent assays). Data sets marked with different letters in **(A, F)** indicate significant differences assessed using one-way ANOVA, followed by Fisher's LSD test ($P < 0.05$). Significant differences in **(B–E)** were determined using a two-tailed Student's *t*-test (*$P < 0.05$; **$P < 0.01$).

lower than LOH2-Flag activity (Figure 4F), consistent with the results of *in vitro* CerS assays with microsomal proteins from *LOH2*-OE #12 and *LOH2*^{S289A,S291A}-OE #18 (Figure 4A). We also constructed vectors driven by the native LOH2 promoter and obtained similar results from *in vivo* CerS assays (Figure S12; Dataset S7). We then generated phosphomimetic mutants (Ser (S) to Asp (D)) and found that LOH2^{S289D,S291D} had significantly higher enzymatic activity than LOH2^{S289A,S291A} (Figure 4F; Dataset S6), indicating that phosphorylation at S289 and S291 increases LOH2 activity. We next evaluated the contributions of the individual C-terminal phosphorylation sites to LOH2 activity by generating single S-to-A mutants. The activity of LOH2^{S289A}-Flag was more severely impaired than that of LOH2^{S291A}-Flag, showing a 92.9% decrease in activity compared with LOH2-Flag, whereas the activity of LOH2^{S291A} was largely normal (Figure 4F). These results

17447909, 0, Downloaded from https://onlinelibrary.wiley.com/doi/10.1111/jipb.70081 by University Of British Columbia, Wiley Online Library on [27/01/2026]. See the Terms and Conditions (https://onlinelibrary.wiley.com/terms-and-conditions) on Wiley Online Library for rules of use; OA articles are governed by the applicable Creative Commons License

suggest that S289 is the more important phosphorylation site for modulating the enzymatic activity of LOH2, consistent with its high conservation across plants and other eukaryotes (Figure S1B).

Because the activity of LOH2^{S289A,S291A} was low, we speculated whether its substrate-binding ability had changed. We therefore examined the *in vitro* affinity of recombinant purified LOH2-His and LOH2^{S289A,S291A}-His toward d18:0 and t18:0 by performing lipid–protein membrane binding assays using filters spotted with various amounts of lipids. Compared with LOH2-His, LOH2^{S289A,S291A}-His showed weaker binding to d18:0 and t18:0 (Figure S13A). Microscale thermophoresis assays also demonstrated binding of palmitoyl CoA to GFP-LOH2 with a dissociation constant (K_d) of 129.4 μM, which was lower than the K_d for binding of palmitoyl CoA to GFP-LOH2^{S289A,S291A} (177.8 μM) (Figure 4G). These results suggest that a lack of phosphorylation at S289 and S291 may partially disrupt substrate binding by LOH2.

We next asked whether phosphorylation at these two sites directly affects the structure of LOH2. We used AlphaFold3 to predict the structures of LOH2 and LOH2-^{S289A,S291A}. We also compared the structures of LOH2 and LOH2^{S289A,S291A} to a previously reported structure for human CerS6 (Pascoa et al., 2024), which was shown to have the same substrate specificity as LOH2. Arabidopsis LOH2 and human CerS6 share very similar 3D structures, as both contain seven transmembrane (TM) helices. The TM2–TM7 barrel of CerS6 resembles a six-TM barrel structure, which is likely optimized for recognition of and reaction with acyl-CoA substrates (Pascoa et al., 2024). Replacement of S289 and S291 with alanine appeared to have little effect on the predicted 3D structure of LOH2 (Figure S13B). However, these two sites are located in the cytoplasmic opening of the central cavity formed by the TM2–TM7 barrel (Figure S13B), and S289 and S291 might therefore affect LOH2 activity by influencing substrate access to the catalytic site.

Phosphorylation reduces the stability of LOH2 but does not alter its subcellular localization

The stability of many proteins is regulated by phosphorylation and dephosphorylation mediated by kinases and phosphatases. For example, in the plant light-signaling pathway, CK2-mediated phosphorylation stabilizes ELONGATED HYPOCOTYL 5 (HY5) and LONG HYPOCOTYL IN FAR-RED LIGHT 1 (HFR1), which positively regulate photosynthesis; however, CK2-mediated phosphorylation also promotes degradation of the negative regulator PHY-INTERACTING FACTOR 1 (PIF1) (Hardtke et al., 2000; Park et al., 2008; Bu et al., 2011). To investigate whether the phosphorylation status of LOH2 affects its protein stability, we examined the intensity of GFP fluorescence in *LOH2*-OE #12 and *LOH2*^{S289A,S291A}-OE #18 leaves by confocal microscopy. The average fluorescence intensity of *LOH2*^{S289A,S291A}-OE #18 leaves was significantly higher than that of *LOH2*-OE #12 leaves (Figure 5A).

To confirm the confocal microscopy results, we extracted total proteins from the same overexpression lines and performed immunoblotting using an anti-HA antibody to detect LOH2-GFP-HA and LOH2^{S289A,S291A}-GFP-HA. The abundance of LOH2^{S289A,S291A}-GFP-HA was 42% higher than that of LOH2-GFP-HA (Figure 5B). These overexpression lines had similar *LOH2* expression levels (Figure 3D), suggesting that the lack of phosphorylation at residues S289 and S291 increases LOH2 stability.

We then investigated whether CKα1 and CKβ1 regulate LOH2 stability. We transfected protoplasts prepared from *LOH2pro:LOH2:GFP:HA* plants with the *CKα1-Flag* and *CKβ1-Flag* constructs and quantified LOH2-GFP-HA abundance by immunoblotting after 16–20 h of incubation. We detected lower levels of LOH2-GFP-HA in protoplasts transfected with *CKα1-Flag* and *CKβ1-Flag* than in control non-transfected protoplasts (Figure 5C), suggesting that CKα1 and CKβ1 reduce LOH2 protein stability *in vivo*. To further explore how CKα1 and CKβ1 affect LOH2 protein stability, we used an anti-ubiquitin (Ub) antibody to detect poly-ubiquitinated LOH2 after transiently expressing *CKα1* and *CKβ1* in *LOH2pro:LOH2:GFP:HA* protoplasts, followed by immunoprecipitation with anti-GFP beads. The abundance of poly-ubiquitinated LOH2 was 39% higher in the presence of CKα1 and CKβ1 (Figure 5D). We also observed a shift in LOH2 mobility, with a larger predicted molecular mass in the presence of CKα1 and CKβ1 (Figure 5D). These results demonstrate that CK2-mediated phosphorylation of LOH2 promotes its polyubiquitination *in vivo*.

Protein turnover is often regulated by the 26S proteasome and autophagy (Isono et al., 2024; Sharma et al., 2024). We therefore treated *LOH2*-OE #12 seedlings with cycloheximide (CHX), a protein synthesis inhibitor, and tested the effects of inhibitors of the 26S proteasome (MG132) or autophagy (concanavalin A (ConA)) on LOH2 turnover. The faster degradation of LOH2 was fully inhibited by MG132 and moderately inhibited by ConA treatment (Figure 5E). Taken together, these data suggest that LOH2 phosphorylated by CK2 is primarily degraded via the 26S proteasome pathway.

Phosphorylation is required for the proper endoplasmic reticulum (ER) localization of Lac1p and Lag1p in yeast (Fresques et al., 2014). We therefore investigated whether manipulating LOH2 phosphorylation would affect its subcellular localization. We prepared protoplasts from *35S:GFP*, *LOH2pro:LOH2:GFP:HA*, *LOH2*-OE #12, and *LOH2*^{S289A,S291A}-OE #18 transgenic plants and transfected them with fluorescent markers for the ER, Golgi apparatus, nucleus, and peroxisome or stained them with MitoTracker Red (to stain mitochondria). We detected GFP fluorescence signals for *LOH2pro:LOH2:GFP:HA*, *35S:LOH2:GFP:HA*, and *35S:LOH2*^{S289A,S291A}*:GFP:HA* in the ER (Figure 5F) and Golgi apparatus (Figure 5G), but very little signal was present in the nucleus (Figure S14A), peroxisomes (Figure S14B), or mitochondria (Figure S14C). Because intact LOH2 and its phosphorylation variants showed identical localization, these

17447909, 0, Downloaded from https://onlinelibrary.wiley.com/doi/10.1111/jipb.70081 by University Of British Columbia, Wiley Online Library on [27/01/2026]. See the Terms and Conditions (https://onlinelibrary.wiley.com/terms-and-conditions) on Wiley Online Library for rules of use; OA articles are governed by the applicable Creative Commons License

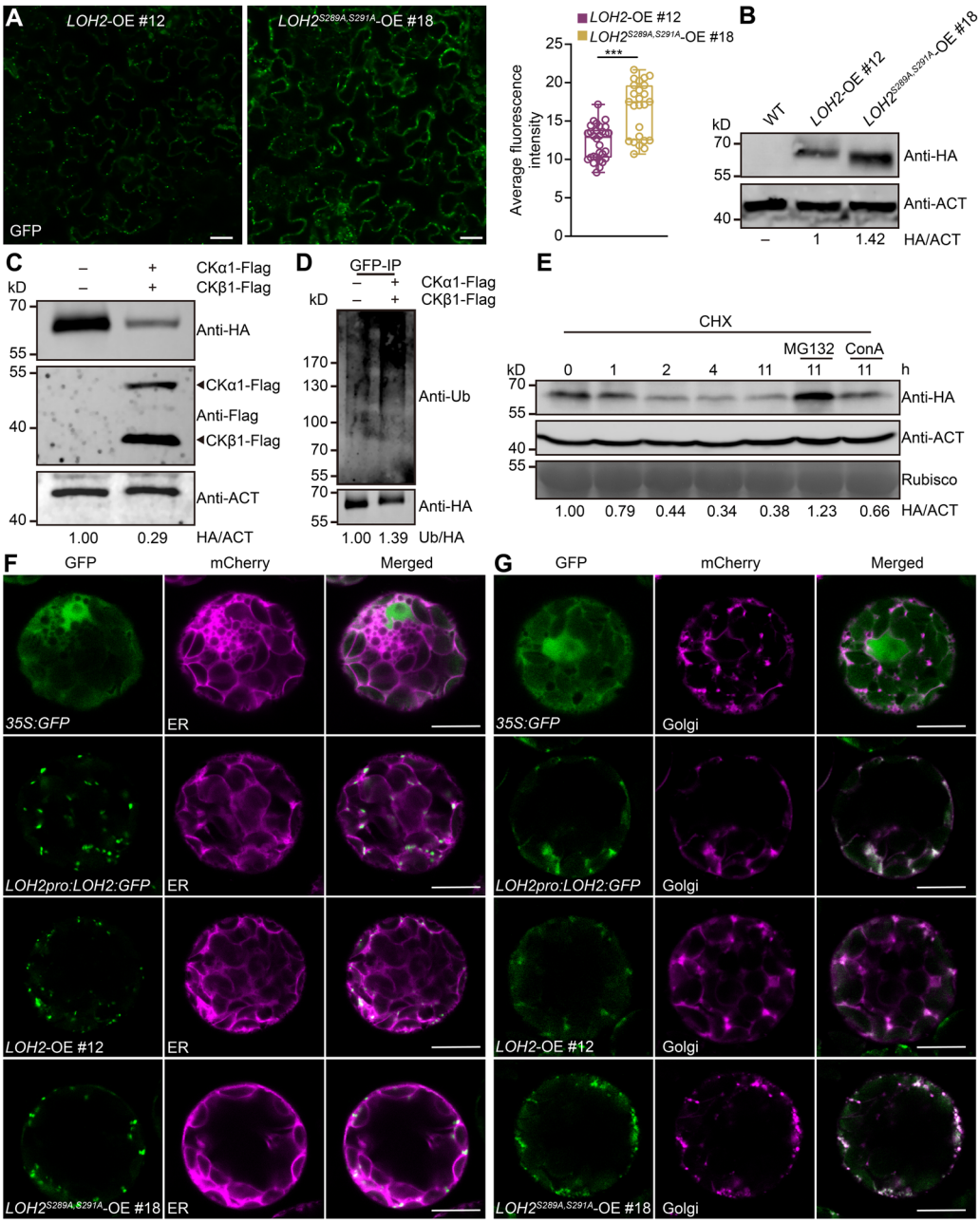

Figure 5. Phosphorylation of LOH2 affects its stability but not its subcellular localization

(A) Confocal live cell images of representative epidermal cells from the leaves of 4-week-old stable transgenic *LOH2*-OE #12 and *LOH2*^{S289A,S291A}-OE #18 plants (left) and the corresponding average fluorescence intensity (right). Scare bar, 20 μm. Data represent means ± standard error (*SE*) ($n \geq 20$ fields per genotype). Significant differences were determined using a two-tailed Student's *t*-test (***$P < 0.001$). **(B)** Immunoblot analysis of LOH2-GFP-HA abundance in 4-week-old wild type (WT), *LOH2*-OE #12, and *LOH2*^{S289A,S291A}-OE #18 plants. Numbers below the blot represent protein abundance after normalization to the loading control (ACTIN). **(C)** Immunoblot analysis showing the effect of CK2 on LOH2-GFP-HA abundance. Protoplasts prepared from *LOH2pro:-LOH2:GFP:HA* plants were transfected with *CKα1-Flag* and *CKβ1-Flag* as indicated. Anti-HA and anti-FLAG antibodies were used for immunoblotting. Numbers below the blot represent LOH2-GFP-HA abundance normalized to ACTIN. **(D)** Effect of CK2 on the ubiquitination of LOH2 *in vivo*. Total proteins were extracted from the protoplasts in **(C)** and enriched using GFP beads. LOH2-GFP-HA was detected with an anti-HA antibody. The poly-ubiquitination of LOH2-GFP-HA was detected with an anti-Ub antibody. Numbers below the blot represent poly-ubiquitinated LOH2-GFP-HA abundance normalized to LOH2-GFP-HA. **(E)** Immunoblot analysis of LOH2 protein abundance in *LOH2*-OE #12 seedlings. Arabidopsis seedlings were grown on half-strength Murashige and Skoog (1/2MS) medium for 10 d, transferred to liquid 1/2MS medium containing 200 μM cycloheximide (CHX) alone or together with 50 μM MG132 or 10 μM concanavalin A (Con A), and incubated for various durations. ACTIN and Rubisco were used as loading controls. Numbers below the blot represent abundance normalized to ACTIN. **(F–G)** Subcellular localization of LOH2. The ER-mCherry marker (CD3-960) **(F)** or the Golgi-mCherry marker **(G)** was transfected into protoplasts prepared from *35S:GFP*, *LOH2pro:LOH2:GFP:HA*, *LOH2*-OE #12, or *LOH2*$^{S289A,\ S291A}$-OE #18 plants. The images were obtained by confocal microscopy 16 h after transfection. Scale bars in **(F–G)**, 10 μm. Quantifications in **(B–E)** were carried out using Adobe Photoshop 2020. Experiments were repeated at least two times with independent samples.

17447909, 0, Downloaded from https://onlinelibrary.wiley.com/doi/10.1111/jipb.70081 by University Of British Columbia, Wiley Online Library on [27/01/2026]. See the Terms and Conditions (https://onlinelibrary.wiley.com/terms-and-conditions) on Wiley Online Library for rules of use; OA articles are governed by the applicable Creative Commons License

results suggest that dephosphorylation at S289 and S291 does not affect the subcellular localization of LOH2.

Phosphorylation enhances LOH2-mediated resistance to FB1

LOH2-overexpressing plants are more resistant to FB1 than WT plants (Luttgeharm et al., 2015). To test whether the phosphorylation status of LOH2 affects LOH2-mediated FB1 resistance, we grew WT, *LOH2*-OE #12, and *LOH2*^{S289A,S291A}-OE #18 seedlings on half-strength Murashige and Skoog (1/2MS) medium containing methanol (Mock) or 0.5 μM FB1 for 10 d. *LOH2*-OE #12 showed much higher resistance to FB1 (Figure 6A, B), and it contained 78.8% lower levels of free LCBs (Figures 6C, S15A; Dataset S8) and 42.2% higher levels of C16 Cers under FB1 treatment compared with the WT (Figure S15B; Dataset S8). Similarly, *LOH2*^{S289A,S291A}-OE #18 seedlings were more resistant to FB1 (Figure 6A, B) and contained 35% lower levels of free LCBs under FB1 treatment compared with the WT (Figure 6C). *LOH2*^{S289A,S291A}-OE #18 showed slightly lower FB1 resistance compared with *LOH2*-OE #12 (Figure 6A, B), and *LOH2*^{S289A,S291A}-OE #18 seedlings contained higher levels of free LCBs and lower levels of C16 Cers (Figures 6C, S15). These results indicate that a lack of LOH2 phosphorylation impairs LOH2-mediated FB1 resistance.

To further investigate the regulatory role of CK2 in sphingolipid metabolism upon FB1 treatment, we grew WT and *cka1 cka2 cka3* seedlings on 1/2MS medium containing methanol (Mock) or 0.5 μM FB1 for 10 d. The *cka1 cka2 cka3* mutant showed increased sensitivity to FB1 (Figure S16A, B), and the FB1-induced accumulation of C16 Cers was markedly lower in the *cka1 cka2 cka3* mutant than in WT plants (Figure S16C). These results demonstrate that FB1-induced accumulation of C16 Cers is dependent on the activity of CK2.

Phosphorylation enhances LOH2-mediated resistance to *Pseudomonas syringae*

We previously reported the different roles of two classes of CerSs in plant immunity and cell death (Zeng et al., 2022). However, little is known about how sphingolipid metabolism is regulated by pathogen infection and how sphingolipids regulate plant responses to pathogen infection, especially at early infection stages. To explore the effects of pathogen infection on sphingolipid metabolism, we inoculated 4-week-old WT plants with *Pseudomonas syringae* pv. *maculicola* (*Psm*DG3) (Dataset S9). Six hours after infection, we

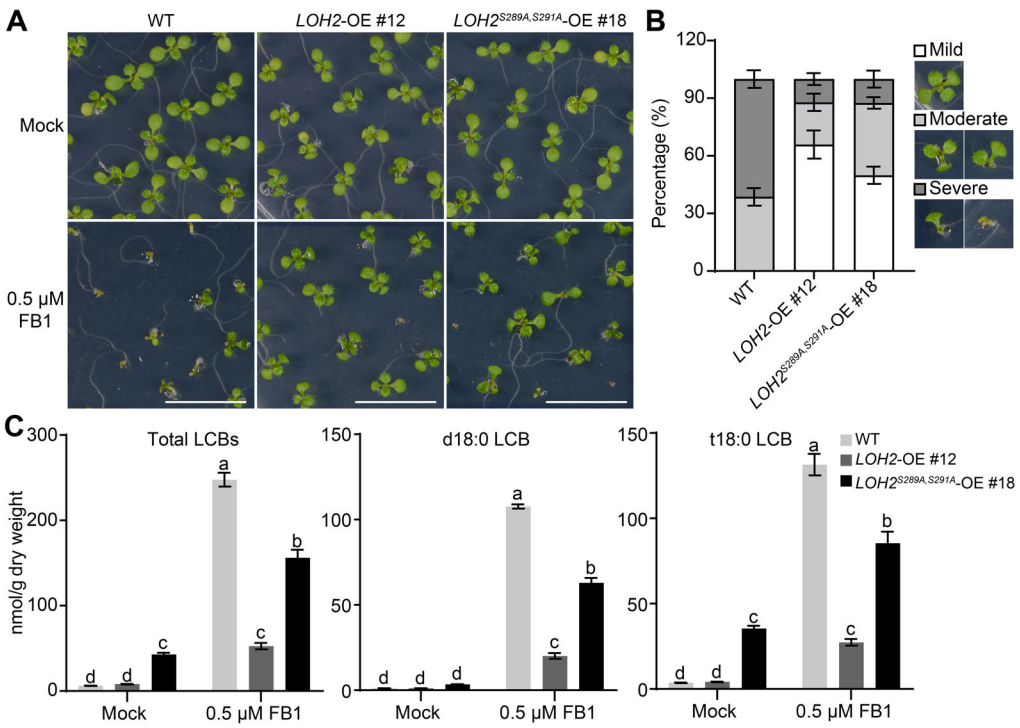

Figure 6. Phosphorylation of LOH2 affects plant sensitivity to FB1

(A) Sensitivity of wild type (WT), *LOH2*-OE #12, and *LOH2*^{S289A,S291A}-OE #18 plants to FB1 treatment. Seedlings were grown on half-strength Murashige and Skoog (1/2MS) medium containing methanol (Mock) or 0.5 μM Fumonisin B1 (FB1) for 10 d and photographed. Scare bar, 1 cm. **(B)** Percentage of seedlings with different levels of FB1 sensitivity after 0.5 μM FB1 treatment. The seedlings were categorized based on the number of cotyledons and true leaves: mild (four), moderate (two or three), and severe (one or zero). Values are means ± *SE* ($n = 4$ biological replicates). At least 30 seedlings per genotype were quantified in each replicate. **(C)** Contents of total long-chain bases (LCBs), d18:0, and t18:0 in the seedlings shown in **(A)**. Values are means ± *SE* ($n = 3$ independent samples). Data sets marked with different letters indicate significant differences among genotypes assessed using one-way ANOVA, followed by Fisher's LSD test ($P < 0.05$).

17447909, 0, Downloaded from https://onlinelibrary.wiley.com/doi/10.1111/jipb.70081 by University Of British Columbia, Wiley Online Library on [27/01/2026]. See the Terms and Conditions (https://onlinelibrary.wiley.com/terms-and-conditions) on Wiley Online Library for rules of use; OA articles are governed by the applicable Creative Commons License

collected plant samples and examined their sphingolipid profiles. The total contents of Cers, C16 Cers, C24 Cers, and C26 Cers were significantly higher upon infection, whereas those of C18 Cers, C20 Cers, and C22 Cers remained largely unchanged (Figure S17A, B). We also measured the expression levels of genes involved in Cer biosynthesis. *LOH2* transcript levels increased significantly after inoculation with *Psm*DG3, whereas those of *LOH1* and *LOH3* were much less responsive (Figure S17C), suggesting that *LOH2* participates in plant responses to pathogen infection. Expression of the SA synthase gene *SA INDUCTION DEFICIENT 2* (*SID2*) was significantly higher 1 h after *Psm*DG3 inoculation than in mock-treated plants. Like *LOH2*, *SID2* was rapidly upregulated from 3 h post inoculation onward (Figure S17D). The expression levels of both *SID2* and *LOH2* peaked at 9 h after inoculation (Figure S17C, D). Notably, *CKB1* expression was also significantly induced by *Psm*DG3 infection (Figure S17E). We therefore speculated whether *Psm*DG3 infection might induce the phosphorylation of LOH2, thereby activating LOH2 at both the transcriptional and post-translational levels.

To test this hypothesis, we inoculated 4-week-old WT, *LOH2*-OE #12, and $LOH2^{S289A,S291A}$-OE #18 plants with *Psm*DG3 to investigate whether LOH2 phosphorylation would affect plant resistance to pathogens. Both *LOH2*-OE #12 and $LOH2^{S289A,S291A}$-OE #18 plants showed enhanced resistance to *Psm*DG3 infection (Figure 7A, B), higher SA contents (Figure 7C), and increased expression of defense-related genes (Figure 7D) compared with the WT. $LOH2^{S289A,S291A}$-OE #18 showed lower resistance to *Psm*DG3 infection compared with *LOH2*-OE #12 (Figure 7A, B). Consistent with their observed phenotypes, $LOH2^{S289A,S291A}$-OE plants accumulated less free SA and expressed defense-related genes at lower levels compared with *LOH2*-OE #12 plants (Figure 7C, D). These results demonstrate that a lack of LOH2 phosphorylation prevents full LOH2-mediated *Psm*DG3 resistance.

Sphingolipids such as d18:0, t18:0, and C16 Cers play important roles in plant responses to pathogens (Magnin-Robert et al., 2015; Zeng et al., 2022); therefore, we analyzed the sphingolipid profiles of 4-week-old WT, *LOH2*-OE #12, and $LOH2^{S289A,S291A}$-OE #18 plants inoculated with *Psm*DG3 (Dataset S10). At 12 h post-infection, WT plants showed a 2.5-fold increase in C16 Cer compared with mock-infected controls. Infected $LOH2^{S289A,S291A}$-OE #18 plants accumulated much higher levels of C16 Cers than infected WT plants but contained lower levels of C16 Cers than infected *LOH2*-OE plants (Figure 7E). Although $LOH2^{S289A,S291A}$-OE #18 plants accumulated more d18:0 and t18:0 than *LOH2*-OE #12 plants after *Psm*DG3 infection (Figure S18), these plants were less resistant to *Psm*DG3 (Figure 7A, B), further highlighting the roles of C16 Cers in plant responses to pathogen infection.

LOH2 is phosphorylated and degraded upon *Psm*DG3 infection

Because *Psm*DG3 infection promoted the expression of *CKB1*, we asked whether inoculation with *Psm*DG3 would induce the phosphorylation of LOH2 (Figure S17E). LOH2 protein abundance was reduced by 60% upon *Psm*DG3 infection (Figure 7F), supporting our findings of CK2-mediated phosphorylation of LOH2 (Figure 5D). We therefore hypothesized that *Psm*DG3 infection induces phosphorylation of LOH2, leading to its degradation. To test this possibility, we inoculated $LOH2^{S289A,S291A}$-OE #18 plants with *Psm*DG3. The levels of $LOH2^{S289A,S291A}$, which cannot be phosphorylated by CK2, remained high and unchanged regardless of inoculation (Figure 7F). This result suggests that *Psm*DG3 infection indeed induces the phosphorylation of LOH2 at S289 and S291 to initiate its protein degradation. Our earlier results showed that CK2-mediated phosphorylation of LOH2 promotes its polyubiquitination (Figure 5E), and we therefore tested whether *Psm*DG3 infection induces the ubiquitination of LOH2. After inoculation with *Psm*DG3, the abundance of poly-ubiquitinated LOH2 increased significantly in *LOH2*-OE#12 (Figure 7G). These results demonstrate that *Psm*DG3 infection induces polyubiquitination of phosphorylated LOH2 *in vivo*.

To further examine the regulatory role of CK2 in sphingolipid metabolism upon *Psm*DG3 infection, we treated WT and *ckα1 ckα2 ckα3* plants with *Psm*DG3. Although no significant differences in phenotypic characteristics or bacterial growth were observed between *ckα1 ckα2 ckα3* mutants and the WT, *Psm*DG3-induced accumulation of C16 Cers was significantly lower in the mutants than in the WT (Figure S19).

Based on these findings, we propose a model for the role of the LOH2–CK2 module in plant–pathogen responses (Figure 7H). Under non-stress conditions, ER- and Golgi-localized LOH2 proteins exist primarily in a low-activity, stable, non-phosphorylated form. This situation allows for the biosynthesis of basal levels of Cers, which are essential for cellular homeostasis. Upon pathogen infection, rapid phosphorylation of LOH2 by CK2 converts it into a highly active form that significantly increases C16 Cer biosynthesis. The accumulation of Cers, in turn, activates SA signaling to enhance plant resistance to pathogens. To ensure Cer homeostasis and prevent excessive Cer accumulation, the phosphorylated form of LOH2 is rapidly degraded via the 26S ubiquitination pathway.

DISCUSSION

In this work, we addressed the critical need for plants to precisely regulate the activity of a Class I CerS to protect against cellular toxicity or excessive immune activation. We demonstrated that the activity and stability of the long-chain CerS enzyme LOH2 are post-translationally regulated through CK2-mediated phosphorylation of two conserved C-terminal serine residues: S289 and S291. This mechanism fine-tunes Cer biosynthesis, modulating plant immune responses and programmed cell death. Notably, our findings reveal a dual role for LOH2 phosphorylation: phosphorylation enhances the enzymatic activity of LOH2 while simultaneously promoting its degradation via the

17447909, 0, Downloaded from https://onlinelibrary.wiley.com/doi/10.1111/jipb.70081 by University Of British Columbia, Wiley Online Library on [27/01/2026]. See the Terms and Conditions (https://onlinelibrary.wiley.com/terms-and-conditions) on Wiley Online Library for rules of use; OA articles are governed by the applicable Creative Commons License

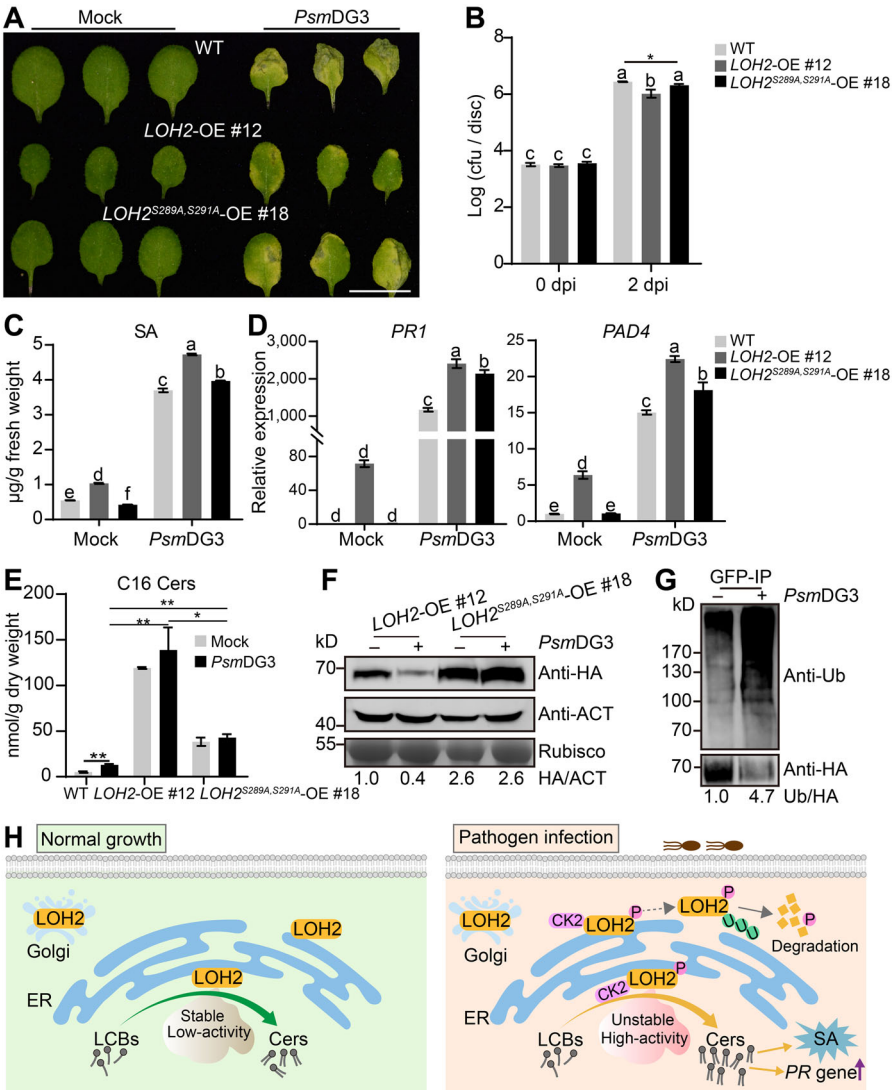

Figure 7. Phosphorylation of LOH2 enhances the resistance of Arabidopsis to *Psm*DG3

(A) Representative photograph of rosette leaves from 4-week-old wild-type (WT), *LOH2*-OE #12, and *LOH2*^{S289A,S291A}-OE #18 plants following mock inoculation with 10 mmol/L $MgSO_4$ (Mock) or inoculation with *Psm*DG3. The plants were photographed 2 d after inoculation. Scale bar, 1 cm. **(B)** Titer of *Psm*DG3 in the leaves of plants shown in **(A)**. Bacterial titer was defined as colony-forming units (CFUs). Values are means ± standard error (*SE*) ($n = 12$ leaves). **(C)** Quantification of free salicylic acid (SA) levels in plants of the indicated genotypes at 24 h post inoculation with *Psm*DG3. Values are means ± *SE* ($n = 3$ independent samples). **(D)** Relative expression levels of the defense-related genes *PR1* and *PAD4* in 4-week-old plants of the indicated genotypes at 24 h post inoculation with *Psm*DG3. *ACT2* transcript levels were used as an internal reference. Expression levels were normalized to WT levels (Mock), which were set to 1. Values are means ± *SE* ($n = 3$). **(E)** Contents of C16 ceramides (Cers) in plants of the indicated genotypes at 12 h post inoculation with *Psm*DG3. Values are means ± *SE* ($n = 3$ independent samples). **(F)** Immunoblot analysis showing the abundance of LOH2-GFP-HA and LOH2^{S289A,S291A}-GFP-HA in *LOH2*-OE #12 and *LOH2*^{S289A,S291A}-OE #18 plants at 6 h post inoculation with *Psm*DG3. ACTIN and Rubisco were used as loading controls. Numbers below the blot represent protein abundance normalized to ACTIN. **(G)** Effect of *Psm*DG3 inoculation on the ubiquitination of LOH2 *in vivo*. Total proteins were extracted from *LOH2*-OE #12 plants at 6 h post inoculation with *Psm*DG3 and enriched with GFP-beads. LOH2-GFP-HA was detected with an anti-HA antibody. Poly-ubiquitinated LOH2-GFP-HA was detected with an anti-Ub antibody. Numbers below the blot represent polyubiquitinated LOH2-GFP-HA abundance normalized to LOH2-GFP-HA. **(H)** Working model for the regulation of LOH2 activity and Cer biosynthesis in response to pathogen infection: Under normal conditions, LOH2 in the endoplasmic reticulum (ER) and Golgi apparatus (Golgi) primarily exists in a low-activity, stable, non-phosphorylated state, producing basal levels of Cers. Upon pathogen infection, LOH2 becomes highly active via phosphorylation by CK2, leading to increased Cer biosynthesis, resulting in the accumulation of SA and increased pathogenesis-related (*PR*) gene expression, thereby enhancing resistance to *Pseudomonas syringae* pv. *maculicola* (*Psm*DG3). To ensure Cer homeostasis in plants, the phosphorylated LOH2 is rapidly degraded via the 26S ubiquitination pathway. Data sets marked with different letters in **(B–D)** indicate significant differences among genotypes assessed using one-way ANOVA, followed by Fisher's LSD test ($P < 0.05$). Asterisks in **(B, E)** indicate a significant difference using a two-tailed Student's *t*-test (*$P < 0.05$; **$P < 0.01$).

ubiquitin–proteasome system, ensuring tight control over sphingolipid homeostasis during pathogen challenges.

Phosphorylation is a ubiquitous regulatory mechanism in eukaryotes, influencing protein function, localization, and stability (Vu et al., 2018; Zhang et al., 2023). Although CerS undergoes phosphorylation in mammals and yeast, the underlying mechanisms are poorly characterized. In yeast, Lac1 and Lag1 can be phosphorylated by Ypk1 at the N terminus and by CK2 at the C

17447909, 0, Downloaded from https://onlinelibrary.wiley.com/doi/10.1111/jipb.70081 by University Of British Columbia, Wiley Online Library on [27/01/2026]. See the Terms and Conditions (https://onlinelibrary.wiley.com/terms-and-conditions) on Wiley Online Library for rules of use; OA articles are governed by the applicable Creative Commons License

terminus, and both of these modifications enhance CerS activity (Fresques et al., 2014; Muir et al., 2014). Moreover, CK2-mediated phosphorylation increases the stability of Lag1 and Lac1 and facilitates their proper localization to the ER (Fresques et al., 2014). Although CK2-mediated phosphorylation also potentiates CerS activity in mammals (Sassa et al., 2016), its effects on protein stability and subcellular localization have not been characterized. Our data demonstrate that CK2 physically interacts with and phosphorylates LOH2 at S289 and S291, enhancing its enzymatic activity but decreasing its stability without affecting its subcellular localization (Figures 2, 4, 5). Therefore, our observations show that the effects of phosphorylation at these highly conserved phosphorylation sites differ between plants and yeast, as CK2-mediated phosphorylation decreases LOH2 stability in Arabidopsis but increases Lag1 and Lac1 stability in yeast. Examining the effect of phosphorylation on the stability of animal CerS enzymes and exploring the conserved and divergent mechanisms involved therefore remain intriguing avenues for future work.

In contrast to LOH2, LOH1 and LOH3 (which also contain the potential CK2 phosphorylation site) showed no interactions with CK2 subunits in plants. Similarly, human CerS3 also harbors potential CK2 phosphorylation sites but is not regulated by CK2 (Sassa et al., 2016). LOH1 and LOH3 have diverged evolutionarily from LOH2 and show functional differences: for example, LOH1 and LOH3 regulate plant growth and development, but LOH2 primarily regulates programmed cell death and immunity (Markham et al., 2011; Bi et al., 2014; Luttgeharm et al., 2015; Zeng et al., 2021). The regulatory mechanisms of LOH1 and LOH3 require further investigation.

Although the promotion of CerS enzymatic activity by CK2-mediated phosphorylation is evolutionarily conserved, the precise molecular mechanisms by which phosphorylation state modulates CerS function remain unclear. Our results reveal that phosphorylation may enhance LOH2 activity in part by facilitating its substrate binding (Figures 4, S13). In addition to phosphorylation, oligomerization can also regulate the activity of mammalian CerS enzymes. For example, mammalian CerS2, CerS5, and CerS6 form heterodimers, with CerS2–CerS5 oligomerization significantly enhancing activity (Mesicek et al., 2010; Laviad et al., 2012). A conserved DXRSDXE oligomerization motif, unique to CerS, is essential for this interaction and for Cer synthesis (Kim et al., 2022). We identified this same conserved motif at the C termini of all three Arabidopsis CerS (LOH1–LOH3), suggesting potential oligomerization-dependent modulation of LOH activity. Furthermore, this motif overlaps with phosphorylation sites in the LOHs, raising the question of whether phosphorylation influences LOH oligomerization and enzymatic activity, a possibility that warrants further investigation.

A particularly intriguing finding is that CK2-mediated phosphorylation also promotes LOH2 turnover. This mechanism creates a feedback loop coupling activation with destabilization, preventing the cytotoxic Cer accumulation observed in *LOH2*-overexpressing plants. Such dual regulation is reminiscent of key immune regulators like NPR1. In systemic acquired resistance, inducers promote NPR1 phosphorylation at Ser11 and Ser15, facilitating both its turnover and transcriptional activity; phosphorylated NPR1 is hypothesized to undergo degradation after interacting with the target promoter (Spoel et al., 2009). A related mechanism was demonstrated for the yeast activator GCN4, in which proteasome inhibition impaired its ability to recruit RNA polymerase II (Lipford et al., 2005). In addition, studies in mammals have shown that CerS1 activity itself influences stability: stress-induced turnover of CerS1 requires its enzymatic activity, as active-site mutations of CerS1 abrogate its degradation (Sridevi et al., 2009). Our results are consistent with this scenario: *Psm*DG3 infection promoted the degradation of phosphorylated (active) LOH2, whereas the low-activity, non-phosphorylatable LOH2 persisted at high levels regardless of inoculation (Figure 7F).

The physiological importance of LOH2 phosphorylation is underscored by the phenotypes of plants expressing the non-phosphorylatable LOH2^{S289A,S291A}. These mutants showed attenuated cell death, reduced SA accumulation, and compromised resistance to FB1 and *Psm*DG3 (Figures 3, 6, 7, S10), suggesting that phosphorylation is essential for the native functions of LOH2, not just its overexpression. The fact that *Psm*DG3 infection itself induces LOH2 phosphorylation and subsequent degradation provides further support for the *in vivo* significance of this regulatory pathway during immune responses.

C16 Cers are known to induce cell death and confer resistance to pathogens. In yeast, Lac1p and Lag1p do not produce C16 Cers, suggesting that C16 Cer biosynthesis may represent an adaptive mechanism in multicellular eukaryotes (Megyeri et al., 2019). The *ckα1 ckα2 ckα3* triple mutant showed reduced FB1- and pathogen-induced C16 Cer accumulation, positioning CK2 upstream of this metabolic shift. Although the mutant did not show altered bacterial growth in our assays, this may reflect the multifaceted regulatory role of CK2 in plant immunity and/or potential functional compensation by other CK2 subunits. Our finding that plant defense pathways regulate sphingolipid biosynthesis through phosphorylation of key enzymes like CerS aligns with a recent study on the phosphoregulation of serine palmitoyltransferase (Li et al., 2023). Given the critical and diverse roles of sphingolipids in plant development and plant–pathogen interactions (Ali et al., 2018; Zhu et al., 2023b) and the conservation of the CK2 phosphorylation motif in CerSs across plant species, manipulation of phosphorylation sites in enzymes like LOH2 and serine palmitoyltransferase via gene editing could have promising applications for fine-tuning plant resistance in crop breeding.

MATERIALS AND METHODS

Plant materials and growth conditions

Arabidopsis thaliana ecotype Col-0 was used as the WT in this study. Plants were grown in soil under a 16-h light/8-h dark photoperiod at 22°C. To generate *LOH2pro:LOH2:GFP:HA* transgenic plants, the genomic *LOH2* sequence, including 2 kb of the endogenous promoter and 2.5 kb of the full-length coding sequence without the stop codon, was cloned into the *EcoRI*

17447909, 0, Downloaded from https://onlinelibrary.wiley.com/doi/10.1111/jipb.70081 by University Of British Columbia, Wiley Online Library on [27/01/2026]. See the Terms and Conditions (https://onlinelibrary.wiley.com/terms-and-conditions) on Wiley Online Library for rules of use; OA articles are governed by the applicable Creative Commons License

and *BamHI* sites of the binary vector *pFGC-35SPPDK* promoter to remove the *35SPPDK* promoter and generate the vector *pFGC-LOH2pro:LOH2:GFP:HA* using the In-Fusion Cloning Kit (catalog number E1101; Vazyme Biotech, Nanjing, China). To generate *35S:LOH2s* (*LOH2* and *LOH2*^{S289A,S291A}*):GFP:HA* transgenic plants, the coding sequence of *LOH2* was amplified and cloned into the *BamHI* sites of the binary vector *pFGC-35SPPDK* using corresponding primers (Table S1). These constructs were transformed into WT plants using the floral-dip method. To generate *LOH2*-OE-*loh2-2* and *LOH2*^{S289A,S291A}-OE-*loh2-2* plants, *LOH2*-OE #12 and *LOH2*^{S289A,S291A}-OE #18 plants were crossed with *loh2-2* mutants. The *ckα1 ckα2 ckα3* triple mutant (N67786) was obtained from the Nottingham Arabidopsis Stock Centre. The *loh2-2* mutant has been described previously (Zeng et al., 2022).

Chemical treatments

For FB1 treatment, seeds were surface-sterilized and sown on 1/2MS medium supplemented with methanol (Mock) or 0.5 μM Fumonisin B1 (F1147; Biofroxx, Einhausen, Germany). After 2 d at 4°C in the dark, plates were transferred to growth chambers under a 16-h light/8-h dark photoperiod at 22°C. Phenotypic characterization and sphingolipid detection were performed after 10 d of germination.

For CHX, MG132, and Con A treatments, 10-d-old Arabidopsis seedlings grown on 1/2MS medium were transferred to liquid 1/2MS medium containing 200 μM CHX (HY–12320; MedChemExpress, Shanghai, China), 200 μM CHX with 50 μM MG132 (M8699; Sigma-Aldrich, Darmstadt, Germany), or 200 μM CHX with 10 μM Con A (A8633; APExBIO, TX, USA). Treatments were administered for the specified durations prior to protein extraction.

Sphingolipid assay

Samples were prepared as described previously (Huang et al., 2022; Liu et al., 2024), with minor modifications. In brief, lyophilized samples (10–30 mg) were extracted in 1 mL of extraction solvent (isopropanol/hexane/water, 55:20:25, v/v/v) containing internal standards (d17:1-sphingosine, d18:1/12:0-ceramide, d18:1/12:0-glucosylceramide, and GM1 ganglioside). The mixtures were incubated at 60°C for 15 min after a 2-min ultrasonic bath. After centrifugation at 12,000 *g* for 30 min, the supernatant was dried using nitrogen gas. The samples were dissolved in 200 μL of methanol and analyzed using a triple quadrupole mass spectrometer (AB SCIEX 4500 Triple Quadrupole LC/MS System). For glycosyl-inositol phosphorylceramide detection, samples dried under nitrogen gas were de-esterified in 33% (w/v) methylamine in ethanol–water (7:3, v/v) for 1 h at 50°C. The samples were then dried and dissolved in 250 μL of methanol–tetrahydrofuran–water (1:2:2, v/v/v) and analyzed using a triple quadrupole mass spectrometer (Agilent 6470 Triple Quadrupole LC/MS System).

Co-immunoprecipitation and BiFC assays

Plasmids for transient transfection were extracted from the relevant *Escherichia coli* cultures using a HiPure Plasmid EF Maxi Kit (P1156–03; Magen, Guangzhou, China). Arabidopsis mesophyll protoplasts were prepared and transfected as described previously (Li et al., 2016). In brief, protoplasts were isolated from 3- to 4-week-old rosette leaves and transfected with the indicated plasmids, and then cultured for 16 h to facilitate protein expression. For Co-IP assays, total proteins were extracted with IP buffer (50 mmol/L Tris–HCl (pH 7.5), 150 mmol/L NaCl, 1 mmol/L EDTA, 10% glycerol, 1% Triton X-100, and 1× Roche EDTA-free protease inhibitor cocktail). For each sample, 30 μL (10%) of lysate was retained as the input fraction, and the remaining supernatant was incubated with anti-GFP beads for 1–3 h at 4°C with gentle rotation. Beads were washed five times with IP buffer containing 0.1% (v/v) Triton X-100, and then eluted in IP buffer at 37°C for 20 min before immunoblot analysis.

For BiFC assays, the full-length coding sequences of *LOH1*, *LOH2*, *LOH3*, *PTPLA*, and *CK2* subunits were cloned into pSATN-nEYFP-C1 (nYFP) or pSATN-cYFP-C1 (cYFP) vectors (Citovsky et al., 2006) and co-transfected into leaf protoplasts. Fluorescence was detected after incubation for 16 h under normal conditions using an SP8 confocal laser scanning microscope (Leica Microsystems GmbH). The *PTPLA-nYFP* and *PTPLA-cYFP* vectors were used as positive controls (Morineau et al., 2016), and empty vectors were co-transformed as negative controls.

Pull-down assay

The pull-down assays were performed as described previously (Wang et al., 2019), with minor modifications. Purified recombinant proteins (GST, GST-CKα1, or GST-CKβ1) were incubated with LOH2-His recombinant protein at 12°C for 2 h with continuous rocking. The mixture was then incubated with glutathione beads (GE Healthcare Bio-sciences AB, Uppsala, Sweden) at 4°C for another 2 h. After centrifugation and supernatant removal, the beads were washed five times with wash buffer (40 mmol/L Tris (pH 8.0), 300 mmol/L NaCl, 10% glycerol, and 0.1% Triton X-100). Bound proteins were used for immunoblotting with an anti-His antibody.

Yeast two-hybrid assay

Yeast two-hybrid assays were performed as described previously (Wang et al., 2023a), with minor modifications. In brief, the open reading frames of *LOH1* and *LOH3* were cloned into the pGBKT7 vector and those of the *CK2* subunits were cloned into pGADT7. All constructs were transformed into yeast strain AH109. Yeast colonies were selected on SD medium lacking Leu and Trp (–L–W) and were then serially diluted and plated onto SD medium without Leu, Trp, His, and Ade (–L–W–H–A) at 28°C for 2 d. The interaction between pGBKT7-p53 and pGADT7-T served as the positive control and pGBKT7-Lam co-expressed with pGADT7-T served as the negative control.

In vitro phosphorylation assay and mass spectrometry analysis

The *in vitro* phosphorylation assay was performed as described previously (Zhou et al., 2022). Human glioblastoma

17447909, 0, Downloaded from https://onlinelibrary.wiley.com/doi/10.1111/jipb.70081 by University Of British Columbia, Wiley Online Library on [27/01/2026]. See the Terms and Conditions (https://onlinelibrary.wiley.com/terms-and-conditions) on Wiley Online Library for rules of use; OA articles are governed by the applicable Creative Commons License

recombinant CK2 (α2β2 tetrameric holoenzyme) was purchased from New England Biolabs (NEB, MA, USA). Recombinant LOH2-His (10 μg) was incubated with CK2 in 10× CK2 reaction buffer (NEB, MA, USA) and 3 μL of 10 mmol/L N6-substituted ATPγS at 30°C for 30 min, followed by supplementation with 1.5 μL of 50 mmol/L p-nitrobenzyl mesylate and additional incubation at 30°C for 1 h. The reactions were terminated by the addition of 5× sodium dodecyl sulfate (SDS) loading buffer. Phosphorylated substrate proteins were detected with a thiophosphate ester-specific antibody (ab92570, 1:5,000; Abcam, Cambridge, UK) after separation by 8%–10% SDS polyacrylamide agarose gel electrophoresis (SDS-PAGE).

For mass spectrometry analysis, recombinant LOH2-His (40 μg) was incubated with human glioblastoma recombinant CK2 (NEB, MA, USA) and then subjected to mass spectrometry.

Protein extraction, trypsin digestion, and LC–MS/MS analysis

Fresh leaf tissues (1 g) from *LOH2*-OE #12 plants were ground into powder in liquid nitrogen and then suspended in ice-cold extraction buffer (0.1 M Tris–HCl (pH 8.0), 10 mmol/L EDTA, 5 mmol/L DTT, 0.9 M sucrose, and protease and phosphatase inhibitors). After mixing with Tris-buffered phenol (pH 8.0), sonication in an ice bath, and centrifugation, the phenol phase was mixed with five volumes of ice-cold methanol with 0.1 M ammonium acetate and incubated at −20°C for 3 h. Precipitated proteins were collected by centrifugation, washed sequentially with cold methanol and acetone, and air-dried. Pellets were resuspended in 50 mmol/L NH_4HCO_3 and 8 M urea, reduced with 10 mmol/L DTT (37°C, 30 min), and alkylated with 40 mmol/L iodoacetamide for 30 min at room temperature in the dark. The solution was diluted with 50 mmol/L NH_4HCO_3 to reduce the urea concentration to 1 M. Protein concentration was quantified using the BCA assay (Thermo Fisher Scientific, MA, USA). Proteins were digested with trypsin (Catalog No. 90057, MS grade; Thermo Fisher, MA, USA) (1/100, w/w) at 37°C for 8 h. The digest was acidified to pH ≤ 3 with trifluoroacetic acid, desalted using Pierce peptide desalting spin columns (Thermo Fisher Scientific, MA, USA), lyophilized, and stored at −20°C for further analysis.

The online phosphoproteome analysis was performed as described previously (Zhang et al., 2022b). Enriched peptides were separated on a C18 analytical column (75 μm × 250 mm, 1.9 μm) using an acetonitrile (ACN) gradient with a flow rate of 300 nL/min. The gradient profile was as follows: 5%–25% ACN, 0–90 min; 25%–35%, 90–105 min; and 35%–85%, 105–120 min. The source voltage was 2.0 kV, and the ion transfer tube temperature was 320°C. Data-dependent acquisition mode was used, with MS1 spectra acquired in the Orbitrap over *m/z* 375–1,500 at 120 K resolution. MS2 spectra were triggered at an intensity threshold of 5.0E4, using higher-energy collisional dissociation at 30% collision energy and 15 K resolution. Peptides were identified using Proteome Discoverer software.

Trypan blue staining

Trypan blue staining was performed as described in Zeng et al. (2021), with minor modifications. In brief, plants were submerged in a trypan blue staining solution consisting of 2.5 mg/mL trypan blue (Sigma-Aldrich, Darmstadt, Germany) in 25% (v/v) lactic acid, 25% (v/v) water-saturated phenol, 25% (v/v) glycerol, and 25% (v/v) distilled water. The samples were immediately heated in a boiling water bath for 2 min, and then destained in chloral hydrate solution for at least 12 h.

Phytohormone content determination

Salicylic acid and SAG were extracted as described previously (Zeng et al., 2021), with minor modifications. In brief, fresh leaf tissues (100–300 mg) were immediately frozen in liquid nitrogen and homogenized using an oscillatory tissue pulverizer (50 Hz, 2 min). Subsequently, 0.9 mL of extraction buffer (2:1:0.002, v/v/v, isopropanol–water–concentrated HCl) with an internal standard (10 ng D_4-SA; Olchemim, Olomouc, Czech Republic) was added. The mixtures were gently mixed for 30 min at 4°C, followed by addition of 1 mL dichloromethane and shaking for another 30 min at 4°C. The mixtures were centrifuged at 13,000 *g* for 5 min, and 1 mL of solvent from the lower phase was dried. The dried samples were dissolved in 200 μL of a solution containing 120 μL of methanol and 80 μL of distilled water and analyzed using a triple quadrupole mass spectrometer (AB SCIEX 4500 Triple Quadrupole LC/MS System).

Real-time quantitative polymerase chain reaction

Total RNA was extracted from leaf tissues using the Plant RNA Kit (R6827–02; Omega Bio–Tek, GA, USA) and reverse-transcribed into first-strand cDNA using HiScript II Q RT SuperMix for quantitative polymerase chain reaction (qPCR) (+gDNA wiper) (R223; Vazyme Biotech, Nanjing, China). Real-time PCR was performed using Genious 2X SYBR Green Fast qPCR Mix (RK21204; ABclonal, Wuhan, China) on a LightCycler 480 System (Roche) under the following cycling conditions: initial denaturation at 95°C for 30 s, followed by 40 cycles of 95°C for 5 s, 60°C for 30 s, and 72°C for 20 s. *ACTIN 2* was used as the internal control gene. The primers used in this study are listed in Table S1.

Ceramide synthase assays

In vitro CerS assays were performed as described previously (Zeng et al., 2021). In brief, LCB/BSA complexes were prepared by combining 100 μM bovine serum albumin (BSA) and 20 μM d18:0 or t18:0 LCBs dissolved in a 2:1 (v/v) ethanol:dimethyl sulfoxide solution. All solutions were standardized to contain 10% (v/v) ethanol:dimethyl sulfoxide (2:1), with LCB/BSA complexes representing a 10× stock solution. The 100-μL reaction mixture contained 20 mmol/L potassium phosphate (pH 7.5), 250 mmol/L sorbitol, 50 μM palmitoyl-CoA (16:0-CoA), 10 μM BSA, 20 μM d18:0 or t18:0, and 10 μg of microsomal protein. Following a 30-min incubation at 37°C, reactions were terminated by addition of 750 μL of methyl-tert-butyl ether (MTBE):methanol (1:1, v/v) and vigorous vortex mixing. Ten

17447909, 0, Downloaded from https://onlinelibrary.wiley.com/doi/10.1111/jipb.70081 by University Of British Columbia, Wiley Online Library on [27/01/2026]. See the Terms and Conditions (https://onlinelibrary.wiley.com/terms-and-conditions) on Wiley Online Library for rules of use; OA articles are governed by the applicable Creative Commons License

picomoles of C12-ceramide internal standard were added, and phase separation was induced by addition of 850 μL of MTBE and 312 μL of water. The MTBE upper layer was removed to a clean tube, evaporated using nitrogen gas, and analyzed on a SCIEX QTRAP 4500 LC/MS System; quantification was performed using SCIEX OS software.

In vivo CerS assays were performed as described previously (Sassa et al., 2016), with minor modifications. *LOH2-Flag*, *LOH2^{S289A}-Flag*, *LOH2^{S291A}-Flag*, and *LOH2^{S289A,S291A}-Flag* plasmids were transformed into protoplasts isolated from *loh2-2* mutant plants. After transfection for 16–20 h, sphingolipids were extracted, and Cers with C16 fatty acid moieties were analyzed on a SCIEX QTRAP 4500 LC/MS System and quantified using SCIEX OS software.

In vitro lipid–protein binding assay

Lipid–protein membrane binding assays were performed as described previously (Zhou et al., 2022). In brief, recombinant LOH2-His and LOH2^{S289A,S291A}-His proteins were purified using Ni Sepharose (17–5318–01; GE Healthcare Bio–Sciences AB, Uppsala, Sweden). Sphingolipids solubilized in chloroform were spotted onto polyvinylidene difluoride membranes, and then incubated at room temperature for 1 h in the dark. The lipid-bound membranes were blocked in Tris-buffered saline (TBS) with 1% (w/v) nonfat milk for 1 h and then incubated with 20 μg LOH2-His or LOH2^{S289A,S291A}-His in blocking buffer for 3 h. The membranes were gently washed three times for 10 min each with TBST (TBS + 0.05% Tween-20). After incubation with an anti-His antibody for 3 h at room temperature, the filters were washed 3 times for 10 min each with TBST and then incubated with a horseradish peroxidase-conjugated secondary antibody for 1 h before immunoblotting.

Microscale thermophoresis assay

Microscale thermophoresis (MST) assays were performed as described previously (Wang et al., 2023b). In brief, plasmids encoding GFP-LOH2 or GFP-LOH2^{S289A,S291A} were transformed into protoplasts isolated from *loh2-2* mutant plants. After 16–20 h of transfection, total proteins were extracted with lysis buffer (50 mmol/L HEPES, pH 7.0, 150 mmol/L NaCl, 5 mmol/L $MgCl_2 \cdot 6H_2O$, 10 mmol/L NaF, 10% glycerol, 0.5 mmol/L DTT, 0.05% Tween-20, and 1× Roche EDTA-free protease inhibitor cocktail). Affinity between whole-cell lysates and palmitoyl CoA was assessed using a Monolith NT.115 instrument (NanoTemper). The palmitoyl CoA ligands were serially 2× diluted from 2.5 mmol/L to 76.3 nM. The data were obtained from three independent repeated experiments, and the results were displayed by GraphPad Prism 8.0.

Protein preparation and immunoblot analysis

Proteins were prepared as described previously (Zhou et al., 2022), with minor modifications. Arabidopsis tissues were homogenized in liquid nitrogen and then resuspended in protein extraction buffer (50 mmol/L Tris–HCl (pH 7.5), 150 mmol/L NaCl, 1 mmol/L EDTA, 10% (v/v) glycerol, 1% (v/v) Triton X-100) supplemented with protease inhibitor cocktail. The lysate was incubated on ice for 30 min, and then centrifuged at 12,000 *g* for 30 min at 4°C. The supernatant was collected for subsequent analysis.

For immunoblot analysis, total proteins were separated by SDS-PAGE and transferred to nitrocellulose membranes (GE Healthcare Bio-sciences AB, IL, USA). Immunoblotting was performed using the following primary antibodies: anti-HA (H6533, 1:5,000; Sigma-Aldrich, Darmstadt, Germany), anti-GFP (B1156, 1:5,000; Biodragon, Jiangsu, China), anti-FLAG (A8592, 1:5,000; Sigma-Aldrich, Darmstadt, Germany), anti-His (12698S, 1:2,000; Cell Signaling Technology, MA, USA), anti-thiophosphate ester (ab92570, 1:5,000; Abcam, Cambridge, UK), and anti-plant actin (R3772–1 P, 1:2,000; Abiocode, CA, USA). Protein bands were detected using an enhanced chemiluminescence system after incubation with species-matched horseradish peroxidase-conjugated secondary antibodies.

Subcellular protein localization

Subcellular protein localization assays were performed as described previously (Li et al., 2016), with minor modifications. An ER mCherry marker (CD3–960; TAIR), a Golgi mCherry marker, a nucleus mCherry marker (ARF4-mCherry), or a peroxisome mCherry marker was transformed by transient expression into protoplasts of *35S:GFP*, *LOH2pro:LOH2:GFP:HA*, *LOH2*-OE #12, and *LOH2^{S289A,S291A}*-OE #18 plants. Mitochondrial localization was visualized using MitoTracker Red staining. Protoplasts of *35S:GFP* plants were transformed as controls. The transfected protoplasts were cultured for 16–20 h at room temperature and observed using an SP8 confocal laser scanning microscope (Leica Microsystems GmbH). The excitation/emission wavelengths were 488 nm/500 to 530 nm for GFP and 561 nm/580 to 630 nm for mCherry.

Pathogen inoculation assay

Culturing and inoculation of *Pseudomonas syringae* pv. *maculicola* ES4326 strain DG3 (*Psm*DG3) were performed as described previously (Zeng et al., 2022), with minor modifications. In brief, the third to fourth leaves of 3- or 4-week-old plants were infiltrated with *Psm*DG3 at an OD_{600} of 0.001 (1.08×10^7 colony-forming units/mL) or 10 mmol/L $MgSO_4$ (Mock). For bacterial growth assays, at least 30 plants per genotype were tested, with six to 12 independent leaf disks harvested at 0 and 2 d post-inoculation. The leaf disks were homogenized in 200 μL of 10 mmol/L $MgSO_4$, and then plated in serial dilutions on King's B medium containing 100 μg/mL streptomycin and 50 μg/mL kanamycin. Bacterial colony-forming units were counted after 2 d of incubation at 28°C.

Statistical analysis

Data are presented as means ± standard error (*SE*). Statistical analyses were performed by one-way ANOVA, followed by Fisher's LSD test ($P < 0.05$), or a two-tailed Student's *t*-test (*$P < 0.05$; **$P < 0.01$; and ***$P < 0.001$). The numbers of biologically independent replicates are shown in the figure legends.

17447909, 0, Downloaded from https://onlinelibrary.wiley.com/doi/10.1111/jipb.70081 by University Of British Columbia, Wiley Online Library on [27/01/2026]. See the Terms and Conditions (https://onlinelibrary.wiley.com/terms-and-conditions) on Wiley Online Library for rules of use; OA articles are governed by the applicable Creative Commons License

Accession numbers

Sequence data discussed in this article can be found in The Arabidopsis Information Resource (https://www.arabidopsis.org) under the following accession numbers: *LOH1* (AT3G25540), *LOH2* (AT3G19260), *LOH3* (AT1G13580), *CKA1* (AT5G67380), *CKA2* (AT3G50000), *CKA3* (AT2G23080), *CKA4* (AT2G23070), *CKB1* (AT5G47080), *CKB2* (AT4G17640), *CKB3* (AT3G60250), *CKB4* (AT2G44680), *PR1* (AT2G14610), and *PAD4* (AT3G52430).

ACKNOWLEDGEMENTS

We thank Wenyang Zhang from Guangdong Key Laboratory for Crop Germplasm Resources Preservation and Utilization, Guangdong Academy of Agricultural Sciences, for technical support in phosphoproteome analysis assays. We thank the Nottingham Arabidopsis Stock Centre (https://arabidopsis.info) for providing the *ckα1 ckα2 ckα3* triple mutant (N67786) and the Arabidopsis Biological Resource Center (https://abrc.osu.edu) for providing *loh2-2* (SALK_018608). This work was supported by the Natural Science Foundation of Guangdong Province (2023A1515012051, 2025A1515010084) and the National Natural Science Foundation of China (32070196).

CONFLICTS OF INTEREST

The authors declare no conflict of interests.

AUTHOR CONTRIBUTIONS

K.Z., H.-Y.Z., and N.Y. conceived the study and wrote the manuscript. K.Z. performed most of the experiments. N.Y. and H.-Y.Z. contributed reagents/materials. K.Z., Y.-L.C., Y.-K.L., and Y.C. performed the sphingolipid detection and analysis. K.Z. and Y.-L.C. performed hormone detection and analysis. K.Z., J.-T.L., Z.-X.L., and J.L. contributed to the BiFC assays. K.Z., Y.-B.Y., and J.-T.L. contributed to the trypan blue staining and pathogen inoculation assays. K.Z. and L.-Y.W. contributed to the subcellular protein localization assays. K.Z. and Z.-X.L. contributed to the mutant identification. K.Z. and S.-K.L. contributed to the generation of transgenic plants. K.Z. and C.Y. contributed to the statistical analyses. All authors have read and approved the contents of this paper.

Edited by: Zhizhong Gong, China Agricultural University, China

Received Oct. 8, 2025; **Accepted** Oct. 18, 2025; **Published** Nov. 30, 2025

REFERENCES

Ali, U., Li, H.H., Wang, X.M., and Guo, L. (2018). Emerging roles of sphingolipid signaling in plant response to biotic and abiotic stresses. Mol. Plant **11:** 1328–1343.

Bi, F.C., Liu, Z., Wu, J.X., Liang, H., Xi, X.L., Fang, C., Sun, T.J., Yin, J., Dai, G.Y., Rong, C., et al. (2014). Loss of ceramide kinase in Arabidopsis impairs defenses and promotes ceramide accumulation and mitochondrial H_2O_2 bursts. Plant Cell **26:** 3449–3467.

Bu, Q.Y., Zhu, L., Dennis, M.D., Yu, L., Lu, S.X., Person, M.D., Tobin, E.M., Browning, K.S., and Huq, E. (2011). Phosphorylation by CK2 enhances the rapid light-induced degradation of phytochrome interacting factor 1 in Arabidopsis. J. Biol. Chem. **286:** 12066–12074.

Cahoon, E.B., Kim, P., Xie, T., González Solis, A., Han, G.S., Gong, X., and Dunn, T.M. (2024). Sphingolipid homeostasis: How do cells know when enough is enough? Implications for plant pathogen responses. Plant Physiol. **197:** kiae460.

Citovsky, V., Lee, L.Y., Vyas, S.C., Glick, E., Chen, M.H., Vainstein, A., Gafni, Y., Gelvin, S.B., and Tzfira, T. (2006). Subcellular localization of interacting proteins by bimolecular fluorescence complementation in planta. J. Mol. Biol. **362:** 1120–1131.

Fresques, T., Niles, B., Aronova, S., Mogri, H., Rakhshandehroo, T., and Powers, T. (2014). Regulation of ceramide synthase by casein kinase 2-dependent phosphorylation in *Saccharomyces cerevisiae*. J. Biol. Chem. **290:** 1395–1403.

Hardtke, C.S., Gohda, K., Osterlund, M.T., Oyama, T., Okada, K., and Deng, X.W. (2000). HY5 stability and activity in Arabidopsis is regulated by phosphorylation in its COP1 binding domain. EMBO J. **19:** 4997–5006.

Huang, L.Q., Li, P.P., Yin, J., Li, Y.K., Chen, D.K., Bao, H.N., Fan, R.Y., Liu, H.Z., and Yao, N. (2022). Arabidopsis alkaline ceramidase ACER functions in defense against insect herbivory. J. Exp. Bot. **73:** 4954–4967.

Isono, E., Li, J.M., Pulido, P., Siao, W., Spoel, S.H., Wang, Z.S., Zhuang, X.H., and Trujillo, M. (2024). Protein degrons and degradation: Exploring substrate recognition and pathway selection in plants. Plant Cell **36:** 3074–3098.

Kim, J.L., Ben-Dor, S., Rosenfeld-Gur, E., and Futerman, A.H. (2022). A novel C-terminal DxRSDxE motif in ceramide synthases involved in dimer formation. J. Biol. Chem. **298:** 101517.

Klimczak, L.J., Collinge, M.A., Farini, D., Giuliano, G., Walker, J.C., and Cashmore, A.R. (1995). Reconstitution of Arabidopsis casein kinase II from recombinant subunits and phosphorylation of transcription factor GBF1. Plant Cell **7:** 105–115.

Laviad, E.L., Albee, L., Pankova-Kholmyansky, I., Epstein, S., Park, H., Merrill, Jr., A.H., and Futerman, A.H. (2008). Characterization of ceramide synthase 2: Tissue distribution, substrate specificity, and inhibition by sphingosine 1-phosphate. J. Biol. Chem. **283:** 5677–5684.

Laviad, E.L., Kelly, S., Merrill, A.H., and Futerman, A.H. (2012). Modulation of ceramide synthase activity via dimerization. J. Biol. Chem. **287:** 21025–21033.

Li, J., Yin, J., Rong, C., Li, K.E., Wu, J.X., Huang, L.Q., Zeng, H.Y., Sahu, S.K., and Yao, N. (2016). Orosomucoid proteins interact with the small subunit of serine palmitoyltransferase and contribute to sphingolipid homeostasis and stress responses in Arabidopsis. Plant Cell **28:** 3038–3051.

Lipford, J.R., Smith, G.T., Chi, Y., and Deshaies, R.J. (2005). A putative stimulatory role for activator turnover in gene expression. Nature **438:** 113–116.

Li, Y., Cao, H.W., Dong, T.T., Wang, X.K., Ma, L., Li, K., Lou, H.Q., Song, C.P., and Ren, D.T. (2023). Phosphorylation of the LCB1 subunit of Arabidopsis serine palmitoyltransferase stimulates its activity and modulates sphingolipid biosynthesis. J. Integr. Plant Biol. **65:** 1585–1601.

Liu, H.Z., Li, Y.K., Chen, Y.L., Zhou, Y., Sahu, S.K., Liu, N.J., Wu, H., Shui, G.H., Chen, Q.F., and Yao, N. (2024). Exploring the plant lipidome: Techniques, challenges, and prospects. Adv. Biotechnol. **2:** 11.

Liu, N.J., Hou, L.P., Bao, J.J., Wang, L.J., and Chen, X.Y. (2021). Sphingolipid metabolism, transport, and functions in plants: Recent progress and future perspectives. Plant Comm **2:** 100214.

17447909, 0, Downloaded from https://onlinelibrary.wiley.com/doi/10.1111/jipb.70081 by University Of British Columbia, Wiley Online Library on [27/01/2026]. See the Terms and Conditions (https://onlinelibrary.wiley.com/terms-and-conditions) on Wiley Online Library for rules of use; OA articles are governed by the applicable Creative Commons License

Lu, S.X., Liu, H.T., Knowles, S.M., Li, J., Ma, L.G., Tobin, E.M., and Lin, C.T. (2011b). A role for protein kinase casein kinase2 alpha-subunits in the Arabidopsis circadian clock. Plant Physiol. **157:** 1537–1545.

Luttgeharm, K.D., Cahoon, E.B., and Markham, J.E. (2016). Substrate specificity, kinetic properties and inhibition by fumonisin B1 of ceramide synthase isoforms from Arabidopsis. Biochem. J. **473:** 593–603.

Luttgeharm, K.D., Chen, M., Mehra, A., Cahoon, R.E., Markham, J.E., and Cahoon, E.B. (2015). Overexpression of Arabidopsis ceramide synthases differentially affects growth, sphingolipid metabolism, programmed cell death, and mycotoxin resistance. Plant Physiol. **169:** 1108–1117.

Magnin-Robert, M., Le Bourse, D., Markham, J., Dorey, S., Clement, C., Baillieul, F., and Dhondt-Cordelier, S. (2015). Modifications of sphingolipid content affect tolerance to hemibiotrophic and necrotrophic pathogens by modulating plant defense responses in Arabidopsis. Plant Physiol. **169:** 2255–2274.

Markham, J.E., Molino, D., Gissot, L., Bellec, Y., Hematy, K., Marion, J., Belcram, K., Palauqui, J.C., Satiat-Jeunemaitre, B., and Faure, J.D. (2011). Sphingolipids containing very-long-chain fatty acids define a secretory pathway for specific polar plasma membrane protein targeting in Arabidopsis. Plant Cell **23:** 2362–2378.

Megyeri, M., Prasad, R., Volpert, G., Sliwa-Gonzalez, A., Galih, A., Aguilera-Romero, A., Riezman, H., Barral, Y., Futerman, A.H., and Schuldiner, M. (2019). Yeast ceramide synthases, Lag1 and Lac1, have distinct substrate specificity. J. Cell Sci. **132:** jcs228411.

Mesicek, J., Lee, H., Feldman, T., Jiang, X.J., Skobeleva, A., Berdyshev, E.V., Haimovitz-Friedman, A., Fuks, Z., and Kolesnick, R. (2010). Ceramide synthases 2, 5, and 6 confer distinct roles in radiation-induced apoptosis in HeLa cells. Cell. Signal. **22:** 1300–1307.

Morineau, C., Gissot, L., Bellec, Y., Hematy, K., Tellier, F., Renne, C., Haslam, R., Beaudoin, F., Napier, J., and Faure, J. (2016). Dual fatty acid elongase complex interactions in arabidopsis. PLoS ONE **11:** e0160631.

Muir, A., Ramachandran, S., Roelants, F.M., Timmons, G., and Thorner, J. (2014). TORC2-dependent protein kinase ypk1 phosphorylates ceramide synthase to stimulate synthesis of complex sphingolipids. eLife **3:** e03779.

Mulekar, J.J., and Huq, E. (2014). Expanding roles of protein kinase CK2 in regulating plant growth and development. J. Exp. Bot. **65:** 2883–2893.

Nakagami, H., Sugiyama, N., Mochida, K., Daudi, A., Yoshida, Y., Toyoda, T., Tomita, M., Ishihama, Y., and Shirasu, K. (2010). Large-scale comparative phosphoproteomics identifies conserved phosphorylation sites in plants. Plant Physiol. **153:** 1161–1174.

Niefind, K., Guerra, B., Ermakowa, I., and Issinger, O. (2001) Crystal structure of human protein kinase CK2: Insights into basic properties of the CK2 holoenzyme. EMBO J. **20:** 5320–5331

Niu, Y.Q., Huang, X.G., He, Z.X., Zhang, Q.Q., Meng, H., Shi, H., Feng, B.M., Zhou, Y.C., Zhang, J.F., Lu, G.D., et al. (2022). Phosphorylation of OsTGA5 by casein kinase II compromises its suppression of defense-related gene transcription in rice. Plant Cell **34:** 3425–3442.

Padmanabha, R., Chen-Wu, J.L., Hanna, D.E., and Glover, C.V. (1990). Isolation, sequencing, and disruption of the yeast CKA2 gene: Casein kinase II is essential for viability in saccharomyces cerevisiae. Mol. Cell. Biol. **10:** 4089–4099.

Park, H.J., Ding, L., Dai, M.Q., Lin, R.C., and Wang, H.Y. (2008). Multisite phosphorylation of Arabidopsis HFR1 by casein kinase II and a plausible role in regulating its degradation rate. J. Biol. Chem. **283:** 23264–23273.

Pascoa, T.C., Pike, A.C.W., Tautermann, C.S., Chi, G., Traub, M., Quigley, A., Chalk, R., Stefanic, S., Thamm, S., Pautsch, A., et al. (2024). Structural basis of the mechanism and inhibition of a human ceramide synthase. Nat. Struct. Mol. Biol. **11:** 39528795.

Roitinger, E., Hofer, M., Köcher, T., Pichler, P., Novatchkova, M., Yang, J.H., Schlögelhofer, P., and Mechtler, K. (2015). Quantitative phosphoproteomics of the ataxia telangiectasia-mutated (ATM) and ataxia telangiectasia-mutated and rad3-related (ATR) dependent DNA damage response in *Arabidopsis thaliana*. Mol. Cell. Proteomics **14:** 556–571.

Rui, L., Kang, P., Shao, J., Lu, M.F., Cui, B.M., Zhao, Y.F., Wang, W., Cai, H.R., Tang, D.Z., Loake, G.J., et al. (2024). The chloroplast-localized casein kinase II alpha subunit, CPCK2, negatively regulates plant innate immunity through promoting S-nitrosylation of SABP3. Plant J. **120:** 552–568.

Salinas, P., Fuentes, D., Vidal, E., Jordana, X., Echeverria, M., and Holuigue, L. (2006). An extensive survey of CK2 α and β subunits in Arabidopsis: Multiple isoforms exhibit differential subcellular localization. Plant Cell Physiol. **47:** 1295–1308.

Sassa, T., Hirayama, T., and Kihara, A. (2016). Enzyme activities of the ceramide synthases CERS2–6 are regulated by phosphorylation in the C-terminal region. J. Biol. Chem. **291:** 7477–7487.

Sharma, I., Talakayala, A., Tiwari, M., Asinti, S., and Kirti, P.B. (2024). A synchronized symphony: Intersecting roles of ubiquitin proteasome system and autophagy in cellular degradation. Plant Physiol. Biochem. **212:** 108700.

Spoel, S.H., Mou, Z.L., Tada, Y., Spivey, N.W., Genschik, P., and Dong, X.N. (2009). Proteasome-mediated turnover of the transcription coactivator NPR1 plays dual roles in regulating plant immunity. Cell **137:** 860–872.

Sridevi, P., Alexander, H., Laviad, E.L., Pewzner-Jung, Y., Hannink, M., Futerman, A.H., and Alexander, S. (2009). Ceramide synthase 1 is regulated by proteasomal mediated turnover. Biochim. Biophys. Acta **1793:** 1218–1227.

Ternes, P., Feussner, K., Werner, S., Lerche, J., Iven, T., Heilmann, I., Riezman, H., and Feussner, I. (2011). Disruption of the ceramide synthase LOH1 causes spontaneous cell death in *Arabidopsis thaliana*. New Phytol. **192:** 841–854.

Vu, L.D., Gevaert, K., and De Smet, I. (2018). Protein language: Post-translational modifications talking to each other. Trends Plant Sci. **23:** 1068–1080.

Wang, G.F., Gao, G.L., Yang, X.N., Yang, X.D., and Ma, P.D. (2022). Casein kinase CK2 structure and activities in plants. J. Plant Physiol. **276:** 153767.

Wang, L.Y., Li, J., Gong, B., Wang, R.H., Chen, Y.L., Yin, J., Yang, C., Lin, J.T., Liu, H.Z., Yang, Y., et al. (2023a). Orosomucoid proteins limit endoplasmic reticulum stress in plants. New Phytol. **240:** 1134–1148.

Wang, X., Ding, Y.L., Li, Z.Y., Shi, Y.T., Wang, J.L., Hua, J., Gong, Z.Z., Zhou, J.M., and Yang, S.H. (2019). PUB25 and PUB26 promote plant freezing tolerance by degrading the cold signaling negative regulator MYB15. Dev. Cell **51:** 222–235.

Wang, Y.J.P., Ju, L.G., Wang, G., Qian, K.Y., Jin, W., Li, M.X., Yu, J.T., Shi, Y.L., Wang, Y.Z., Zhang, Y., et al. (2023b). DNA polymerase POLD1 promotes proliferation and metastasis of bladder cancer by stabilizing MYC. Nat. Commun. **14:** 2421.

Wei, P.L., Demulder, M., David, P., Eekhout, T., Yoshiyama, K.O., Nguyen, L., Vercauteren, I., Eeckhout, D., Galle, M., De, et al. (2021). Arabidopsis casein kinase 2 triggers stem cell exhaustion under al toxicity and phosphate deficiency through activating the DNA damage response pathway. Plant Cell **33:** 1361–1380.

Xie, T., Fang, Q., Zhang, Z.K., Wang, Y.F., Dong, F.T., and Gong, X. (2023). Structure and mechanism of a eukaryotic ceramide synthase complex. EMBO J. **42:** e114889.

Zeng, H.Y., Bao, H.N., Chen, Y.L., Chen, D.K., Zhang, K., Liu, S.K., Yang, L., Li, Y.K., and Yao, N. (2022). The two classes of ceramide synthases play different roles in plant immunity and cell death. Front. Plant Sci. **13:** 824585.

Zeng, H.Y., Li, C.Y., and Yao, N. (2020). Fumonisin B1: A tool for exploring the multiple functions of sphingolipids in plants. Front. Plant Sci. **11:** 600458.

17447909, 0, Downloaded from https://onlinelibrary.wiley.com/doi/10.1111/jipb.70081 by University Of British Columbia, Wiley Online Library on [27/01/2026]. See the Terms and Conditions (https://onlinelibrary.wiley.com/terms-and-conditions) on Wiley Online Library for rules of use; OA articles are governed by the applicable Creative Commons License

Zeng, H.Y., Liu, Y., Chen, D.K., Bao, H.N., Huang, L.Q., Yin, J., Chen, Y.L., Xiao, S., and Yao, N. (2021). The immune components ENHANCED DISEASE SUSCEPTIBILITY 1 and PHYTOALEXIN DEFICIENT 4 are required for cell death caused by overaccumulation of ceramides in Arabidopsis. Plant J. **107:** 1447–1465.

Zeng, H.Y., and Yao, N. (2022). Sphingolipids in plant immunity. Phytopathol. Res. **4:** 20.

Zhang, W.J., Zhou, Y.W., Zhang, Y., Su, Y.H., and Xu, T.D. (2023). Protein phosphorylation: A molecular switch in plant signaling. Cell Rep. **42:** 112729.

Zhang, W.Y., Lai, C.K., Huang, W.J., Li, W.Y., Wu, S.W., Kong, Q., Hopkinson, A.C., Fernie, A.R., Siu, K.W.M., and Yan, S.J. (2022b). An eco-friendly, low-cost, and automated strategy for phosphoproteome profiling. Green Chem. **24:** 9697–9708.

Zhang, Z.C., Yang, W.X., Chu, Y.L., Yin, X.T., Liang, Y.Q., Wang, Q.P., Wang, L., and Han, Z.F. (2022a). AtHD2D, a plant-specific histone deacetylase involved in abscisic acid response and lateral root development. J. Exp. Bot. **73:** 7380–7400.

Zhang, Z.K., Fang, Q., Xie, T., and Gong, X. (2024). Mechanism of ceramide synthase inhibition by fumonisin B1. Structure **32:** 1419–1428.

Zhou, Y., Zhou, D.M., Yu, W.W., Shi, L.L., Zhang, Y., Lai, Y.X., Huang, L.P., Qi, H., Chen, Q.F., Yao, N., et al. (2022). Phosphatidic acid modulates MPK3- and MPK6-mediated hypoxia signaling in Arabidopsis. Plant Cell **34:** 889–909.

Zhu, J., Wang, W.S., Yan, D.W., Hong, L.W., Li, T.T., Gao, X., Yang, Y.H., Ren, F., Lu, Y.T., and Yuan, T.T. (2023a). CK2 promotes jasmonic acid signaling response by phosphorylating MYC2 in Arabidopsis. Nucleic Acids Res. **51:** 619–630.

Zhu, X.M., Li, L., Bao, J.D., Wang, J.Y., Daskalov, A., Liu, X.H., Del Poeta, M., and Lin, F.C. (2023b). The biological functions of sphingolipids in plant pathogenic fungi. PLoS Pathog. **19:** e1011733.

SUPPORTING INFORMATION

Additional Supporting Information may be found online in the supporting information tab for this article: http://onlinelibrary.wiley.com/doi/10.1111/jipb.70081/suppinfo

Figure S1. Potential phosphorylation sites in the C-terminal regions of LOHs
Figure S2. Phylogenetic tree of CerSs from plants, animals, and yeast
Figure S3. Identification of the *ckα1 ckα2 ckα3* triple mutant
Figure S4. Bimolecular fluorescence complementation assays for the interactions of LOH2 with CKα2, CKα3, CKα4, CKβ2, CKβ3, and CKβ4
Figure S5. Identification of *LOH2pro:LOH2:GFP:HA* plants
Figure S6. Bimolecular fluorescence complementation and yeast two-hybrid assays for interactions between LOH1, LOH3, and CK2
Figure S7. Generation of LOH2-overexpression lines and identification of LOH2 phosphorylation sites
Figure S8. Phosphorylation of LOH2 affects sphingolipid metabolism
Figure S9. Phosphorylation of LOH2 affects cell death and *PR1* expression
Figure S10. Complementation assays demonstrating the function of LOH2 and LOH2^{S289A,S291A}
Figure S11. Detection of LOH2 activity in *LOH2*-OE #10 and *LOH2*^{S289A,S291A}-OE #7 plants
Figure S12. Phosphorylation of LOH2 promotes its enzymatic activity
Figure S13. Phosphorylation of LOH2 may affect its binding affinity to substrates
Figure S14. Subcellular localization of LOH2 and LOH2^{S289A,S291A}
Figure S15. d18:1, t18:1, and C16 Cer contents in WT, *LOH2*-OE #12, and *LOH2*^{S289A,S291A}-OE #18 plants in response to FB1 treatment
Figure S16. CK2 negatively regulates FB1-induced C16 Cers accumulation
Figure S17. *Psm*DG3 infection induces C16 Cers accumulation and high levels of *LOH2* and *CKB1* expression
Figure S18. d18:0 and t18:0 contents in WT, *LOH2*-OE #12, and *LOH2*^{S289A,S291A}-OE #18 plants post inoculation with *Psm*DG3
Figure S19. CK2 negatively regulates *Psm*DG3-induced C16 Cers accumulation
Table S1. Primers used in this study
Dataset S1. Sphingolipid profiles of 4-week-old WT and *ckα1 ckα2 ckα3* plants
Dataset S2. Phosphoproteins and phosphorylation sites identified in *LOH2*-OE#12 plants
Dataset S3. Sphingolipid profiles of 4-week-old WT, *LOH2*-OE #12, and *LOH2*^{S289A,S291A}-OE #18 plants
Dataset S4. Sphingolipid profiles of 4-week-old WT, *loh2-2*, *LOH2*-OE-*loh2-2,* and *LOH2*^{S289A,S291A}-OE-*loh2-2* plants
Dataset S5. Sphingolipid profiles in the protoplasts of *LOH2pro:-LOH2:GFP:HA* transfected with plasmid empty vector or CK2 (*CKα1-Flag* and *CKβ1-Flag*)
Dataset S6. Ceramide contents in protoplasts of *loh2-2* transfected with plasmids encoding LOH2-Flag, LOH2^{S289A,S291A}-Flag, LOH2^{S289D,S291D}-Flag, LOH2^{S289A}-Flag, or LOH2^{S291A}-Flag
Dataset S7. Ceramide contents in the protoplasts of *loh2-2* transfected with plasmids encoding LOH2pro:LOH2:GFP or LOH2pro:LOH2^{S289A,S291A}:GFP
Dataset S8. Sphingolipid profiles of WT, *LOH2*-OE #12, and *LOH2*^{S289A,S291A}-OE #18 after FB1 treatment
Dataset S9. Sphingolipid profiles of WT plants 6 h post inoculation with *Psm*DG3
Dataset S10. Sphingolipid profiles of WT, *LOH2*-OE #12, and *LOH2*^{S289A,S291A}-OE #18 12 h post inoculation with *Psm*DG3

Scan the QR code to view JIPB on WeChat (WeChat: **jipb1952**)

Scan the QR code to view JIPB on X (X: **@JIPBio**)

Scan the QR code to view JIPB on Bluesky (Bluesky: **jipb.bsky.social**)

17447909, 0, Downloaded from https://onlinelibrary.wiley.com/doi/10.1111/jipb.70081 by University Of British Columbia, Wiley Online Library on [27/01/2026]. See the Terms and Conditions (https://onlinelibrary.wiley.com/terms-and-conditions) on Wiley Online Library for rules of use; OA articles are governed by the applicable Creative Commons License